Computers in Biology and Medicine 96 (2018) 52–68

Contents lists available at ScienceDirect

Computers in Biology and Medicine

journal homepage: www.elsevier.com/locate/compbiomed

Left atrial appendage segmentation and quantitative assisted diagnosis of atrial fibrillation based on fusion of temporal-spatial information

Cheng Jin [a,b], Jianjiang Feng [a,*], Lei Wang [a], Heng Yu [a], Jiang Liu [a], Jiwen Lu [a], Jie Zhou [a]

[a] Department of Automation, Tsinghua University, Beijing, China
[b] Department of Technology, Qiqihar Medical University, Qiqihar, China

ARTICLE INFO

Keywords:
Atrial fibrillation (AF)
4D-CT
Left atrial appendage(LAA)
Multi-phase segmentation
Temporal-spatial information

ABSTRACT

In this paper, we present an approach for left atrial appendage (LAA) multi-phase fast segmentation and quantitative assisted diagnosis of atrial fibrillation (AF) based on 4D-CT data.

We take full advantage of the temporal dimension information to segment the living, flailed LAA based on a parametric max-flow method and graph-cut approach to build 3-D model of each phase. To assist the diagnosis of AF, we calculate the volumes of 3-D models, and then generate a "volume-phase" curve to calculate the important dynamic metrics: ejection fraction, filling flux, and emptying flux of the LAA's blood by volume. This approach demonstrates more precise results than the conventional approaches that calculate metrics by area, and allows for the quick analysis of LAA-volume pattern changes of in a cardiac cycle. It may also provide insight into the individual differences in the lesions of the LAA. Furthermore, we apply support vector machines (SVMs) to achieve a quantitative auto-diagnosis of the AF by exploiting seven features from volume change ratios of the LAA, and perform multivariate logistic regression analysis for the risk of LAA thrombosis.

The 100 cases utilized in this research were taken from the Philips 256-iCT. The experimental results demonstrate that our approach can construct the 3-D LAA geometries robustly compared to manual annotations, and reasonably infer that the LAA undergoes filling, emptying and re-filling, re-emptying in a cardiac cycle. This research provides a potential for exploring various physiological functions of the LAA and quantitatively estimating the risk of stroke in patients with AF.

1. Introduction

Thrombotic diseases have become a serious threat to human life and health. About 80% of the cardiogenic thrombi navigate to the brain with the coursing blood, which causes strokes [1]. The cardiogenic thrombi (Fig. 1 a–c) occur mainly in the left atrial appendage (LAA). In the case of atrial fibrillation (AF), the volume of LAA increases and its systolic function does not work properly, which leads to outlet obstruction and blood stasis, and eventually induces thrombosis [1]. The LAA is a cardiac substructure that is above the left ventricle (LV) and connected to the left atrium (LA). Its shape is highly variable, often tubular, hooked and with a few lobes. Its size varies from 1 to 19 cm^3 [2]. The LAA also has many physiological functions, such as the secretion of atrial natriuretic peptides (ANP).

Computed tomography (CT) is one of the most advanced medical imaging diagnosis tools. For cardiovascular disease, it can greatly assist clinicians to obtain the anatomical information of the LAA and predict the risk of thrombosis [3] (Fig. 1 c).

Owning to the LAA's small and variable structure, it is both challenging and rewarding to study it based on CT data (Fig. 1), and few researchers have focused on LAA in the image processing domain. Most existing segmentation algorithms are applied to the analysis of a single phase instead of the entire cardiac cycle. There is no automated LAA segmentation approach for 4-D CT data. In order to systematically describe the morphological structure of the LAA, we need to study the entire cardiac cycle. To this end, this research proposes a series of approaches for multi-phase segmentation. Then, we calculate the volume of non-rigid LAA based on the segmentation result. Furthermore, some important metrics are calculated for the diagnosis of AF. Specifically, we leverage the left atrial appendage ejection fraction (LAA-EF), left atrial appendage peak emptying flux (LAA-PEF), and left atrial appendage peak filling flux (LAA-PFF) as indicators of LAA abnormity and AF [4].

The main steps and contributions of our proposed approach are the following:

* Corresponding author.
E-mail address: jfeng@mail.tsinghua.edu.cn (J. Feng).

https://doi.org/10.1016/j.compbiomed.2018.03.002
Received 2 December 2017; Received in revised form 22 February 2018; Accepted 5 March 2018

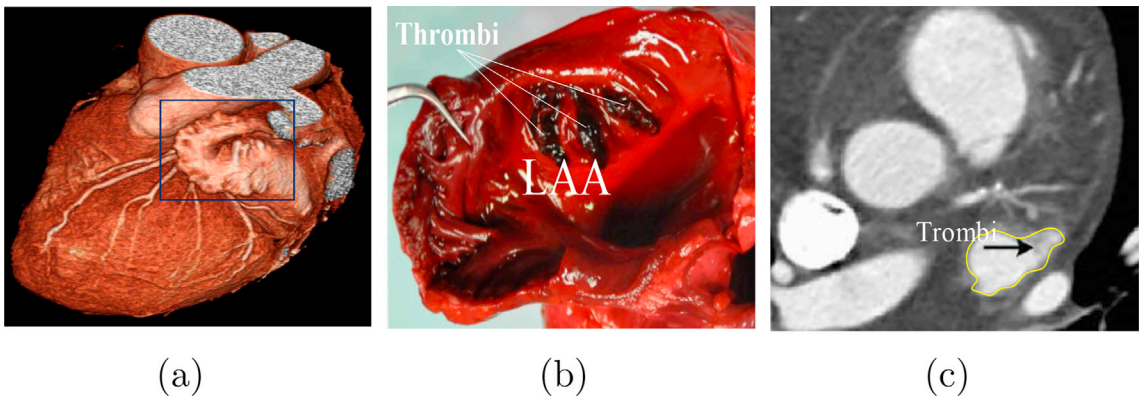

Fig. 1. The LAA, LAA thrombi and an axial CT slice with the LAA. (a) Volume rendering of a heart with the LAA marked by a rectangle, (b) LAA thrombi, (c) An axial CT slice with the LAA marked by a yellow border. (For interpretation of the references to color in this figure legend, the reader is referred to the Web version of this article.)

- We propose a new approach for single phase LAA segmentation without using explicit shape models. Our approach can detect the tips and lobes of the LAA precisely which are missed in most previous research [5–7].
- We propose a fast multi-phase LAA segmentation approach based on 4-D CT data to obtain motion information, which has not been discussed in previous studies. In the patient's CT examination, we find that there is no radical change in the size and position of the LAA between adjacent phases, which we call temporal continuity. We segment the images of all scan sequences iteratively using a graph-cut with the initial seed generated by the previous phase segmentation result. In particular, after the LAA phase with the biggest volume (45% phase) segmented, we generate the initial seed points for its adjacent phases by checking the prior segmentation mask and the image intensity. We determine that the seed points are adequate such that the graph-cut can achieve competitive performance for our multi-phase segmentation task. This process is carried out iteratively until all scan sequences are segmented.
- We calculate the LAA volume of each phase and generate the "volume-phase" curve, which clearly demonstrates that the LAA undergoes filling, emptying, and then re-filling, re-emptying in the entire cardiac cycle. We also screen out the individual differences in lesions of LAA, such as the LAA "stunning" [8].
- We calculate the important dynamic metrics quickly and non-invasively as indicators of LAA abnormity and AF: LAA-EF, LAA-PEF, LAA-PFF. These metrics are calculated by volume, instead of area, which is frequently used in clinical medicine [9]. Furthermore, we apply support vector machine (SVM) to achieve quantitative auto-diagnostics of AF by exploiting seven features of patients' data, and perform multivariate logistic regression analysis for LAA thrombi. This can be a new application of 4-D CT.

The 100 cases utilized in this research were taken from the Philips 256-iCT. The experimental results demonstrate that our approach can construct muti-phase 3-D LAA geometries robustly compared to manual annotations, and generate the "volume-phase" curve to calculate the key function metrics of the LAA. This research provides a potential for studying various physiological functions of the LAA and quantitatively estimating the risk of stroke in patients with AF.

2. Related work

The current work focuses on single phase LAA segmentation using generative model-based approaches. Researchers generally consider the LAA as a part of the left atrium (LA). Zheng *et al.* [5] segmented the entire LA using a multi-part model. They only used a smooth mesh to encase the LAA roughly, but the C-arm CT data they used did not embody the details of LAA, such as the lobes on LAA. Grasland-Mongrain *et al* [6,7]. segmented the LAA by shape-constraints [10]. In this study, the researchers encountered a problem in segmenting the tips of the LAA [6,7] owing to the vagueness of the shape model.

The generative model-based approaches [5,10] cannot deal with the lobes on LAA which are of great clinical significance. A non-model approach is preferred because it is generally driven by the image itself without explicit shape constraints. We could have applied 3-D region-growing [11] to segment the LAA in the bounding box which is simpler and faster, however the segmentation results (Fig. 2 a, b) are not satisfactory because of:

- The interference of the left superior pulmonary vein (LSPV) and the left circumflex branch (LCX) which are adjacent to the LAA;
- The crimping and adhesion of lobes on LAA.

In comparison, our approach solves these problems because it takes full advantage of the continuity of the topological relationships between slices and between phases (Fig. 2 c).

Graph-cut [12] is also a widely used approach. However, this approach is cumbersome because the user needs to mark the seeds of the foreground and background. In addition, it is challenging to determine the value of the parametric λ which has a strong impact on the final result. In fact, a single λ value can not guarantee competitive results under all image conditions. Instead of finding the optimal λ, some work in computer vision [13,14] generated a pool of segmentation proposals using parametric max-flow/min-cut solver [15]. Parametric max-flow can solve the max-flow/min-cut problem with a set of λ values while max-flow in graph-cut solves the problem with a single λ value. By ranking all proposals in the pool, they have achieved competitive performance in vision tasks such as object segmentation.

Inspired by this work based on parametric max-flow, we have proposed a new discriminative model-based approach for single phase LAA segmentation on computed tomography angiography (CTA) data in our previous study [16]. It is a three-step process. After obtaining a bounding box containing the LAA, we first generate a segmentation pool for each slice by setting different seed hypotheses and different λ values. Then, we rank all proposals in each pool and select the best one. Finally, we merge all selected 2-D results using spatial continuity and build the 3-D model. This method can handle large shape variations and almost all image conditions, while it segments only a single phase when the LAA has the largest volume [16].

We segment the LAA slice by slice when dealing with single phase volume. There are two reasons. First, the 3-D combination of relations of seeds is cumbersome, based on the entire 3-D volume and cannot be processed in parallel, which slows down the calculation speed; second, the 2-D preliminary segmented results can be cross-checked according to

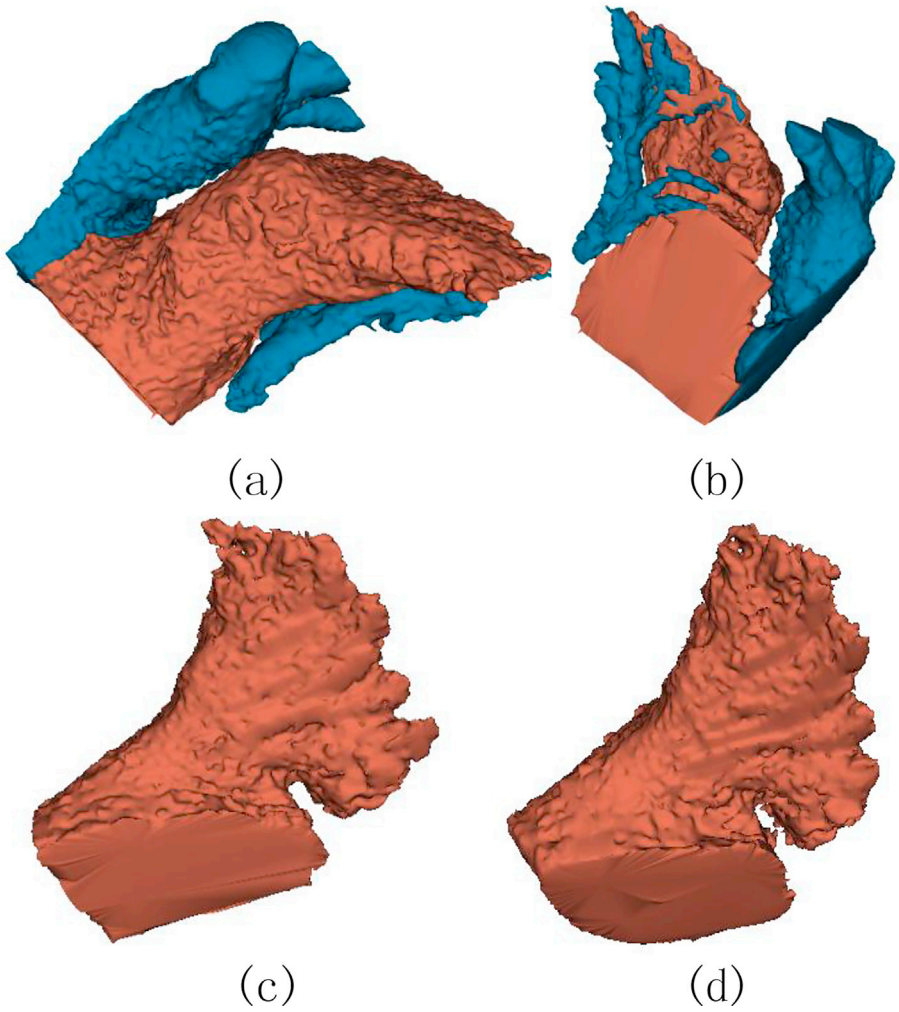

Fig. 2. The model of LAA segmentation with the LSPV and LCX marked in blue. (a) and (b) The results obtained by using 3-D region-growing approach. (c) The result obtained by using our proposed approach, (d) Ground truth. (For interpretation of the references to color in this figure legend, the reader is referred to the Web version of this article.)

the topological relations for accurate segmentation. We also adopt a similar approach in the multi-phase segmentation, which fully utilizes the topological relations between multi-phase volumes in the entire cardiac cycle.

Multi-phase segmentation based on 4-D data has achieved great success in medical image analysis such as coronary registration [17], strain estimation [18] and ventricle wall motion analysis [19]. Müller *et al* [20]. defined an indicator of LV dyssynergy using the ejection fraction and the systolic dyssynergy index derived from the multi-phase segmentation results. Gomez *et al* [19]. reconstructed the 4-D blood flow over the entire ventricle in heart disease by analyzing the ventricle wall motion and blood velocity based on 4-D ultrasound segmentation.

The shape and size of the LAA are changing over time. 4-D data can provide real-time information for clinical diagnosis. Electrocardiogram (ECG) can realize the diagnosis of AF well, but it cannot directly reflect the specific changes of the structure and function of the organs causing AF. Echocardiography can evaluate the LAA function of patients with AF, but its vision is narrow, the spatial resolution is relatively low, and the advanced transesophageal echocardiography(TEE) is invasive in fact. The proposed approach is based on 4D-CT with a retrospective ECG gating technique, which is a beneficial supplement to both. It can measure the LAA blood flow in each stage of an entire cardiac cycle, and predict the risk of causing thrombosis in AF [21]. This research has opened a new path for exploring the various physiological functions of the LAA.

3. LAA segmentation

In order to obtain accurate and efficient segmentation of 4-D LAA data, we first segment the single phase LAA with the largest volume, based on the ranking of 2-D segmentation proposals. According to [22], we selected 45% phase because LAA generally has the largest volume at this phase. Considering that patients are almost lying still during a quick CT examination, we take advantage of the fact that owing to temporal continuity, the size and position changes of the LAA between adjacent phases (Fig. 3) are fairly slight. We segment the LAA of all scan sequences iteratively using graph-cut and the initial seeds are generated by the segmentation result of the previous phase. After a single phase LAA segmentation, we check the single phase segmentation mask and its adjacent image intensity to generate the initial seed points for the next phases. We determine that the seed points are adequate because of temporal continuity. This process is carried out iteratively until all scan sequences are segmented.

3.1. Single-phase 3-D LAA segmentation

Forasmuch as the great anatomical changes of the LAA, and the obstructions to set the optimal value of λ in graph-cut [12]. We propose an approach based on the ranking of 2-D segmentation proposals for precise single-phase LAA segmentation. After obtaining the bounding box of the LAA, we use a three-step process (Fig. 4) to segment the single-phase LAA:

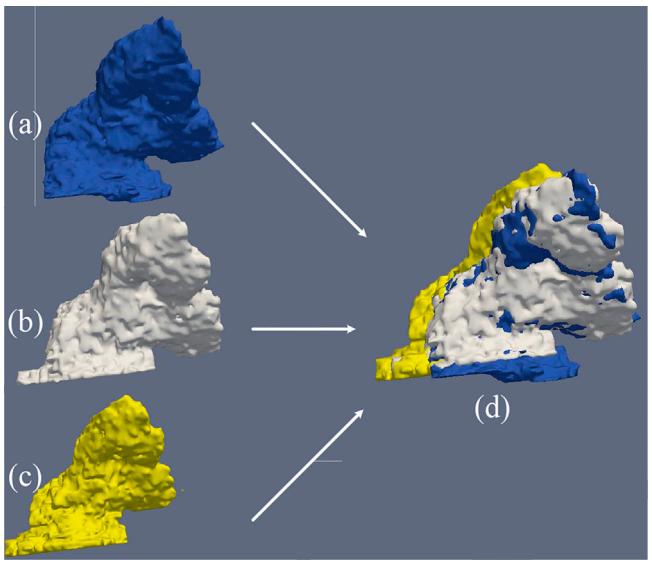

Fig. 3. The LAA fusion of adjacent phases. (a) The LAA of 40% phase. (b) The LAA of 45% phase. (c) The LAA of 50% phase. (d) The fusion result.

of LAA is the largest, at the diagonal corners of a rectangle that contains the LAA closely. One of the last axial slices where the LAA disappears). We only choose the 45% phase because the LAA volume is generally the largest at this phase and there is no significant change in the LAA position among different phases. We enlarge the bounding box by 10% for all sequences to ensure it fully contains the LAA.

3.1.1. *Generating segmentation pool*

We set different foreground and background seed hypotheses and λ values to generate the segmentation pool for each axial slice of the LAA,[1] A segmentation pool is a series of proposals with a high probability of including competitive segmentations. For foreground seeds, we use sets of pixels that form small solid squares. We just place them automatically in a rectangular grid, in a simpler way than [14,15]. For background seeds, we first use the set of pixels that cover full image borders. In a few slices, the LAA is connected to the LA which covers the left and bottom image borders. We also use a set of pixels just covering the right and top image borders. Fig. 6 shows our seed hypotheses. For each seed hypothesis, we set 20 different λ values ranging from 0 to 300. The segmentation generation problem can be solved by a parametric max-flow method. In the next section, we will briefly introduce parametric max-flow.

Image segmentation can be considered as a binary labeling problem

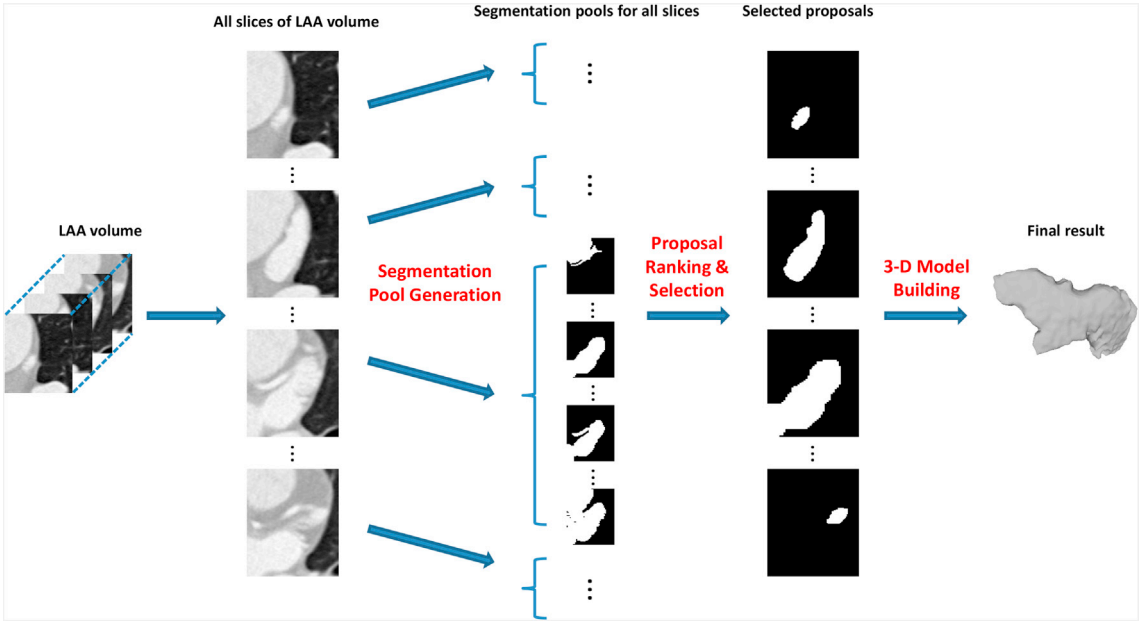

Fig. 4. Flowchart of single-phase LAA segmentation. After obtaining the LAA volume (bounding box containing LAA), a segmented scheme pool is generated for each axial slice. Then, ranked all the proposals in each pool and choose the best one for each slice. Finally, we merge all the selected 2-D schemes according to spatial continuity to generate the 3-D model.

- A pool of segmentation schemes are generated by setting different λ values and seed hypotheses for each axial slice;
- The schemes in each pool are ranked according to the mid-level characteristics and the best scheme is selected for each segmented slice.
- 3-D LAA model was established by merging all the two dimensional schemes, and the spatial continuity of adjacent slices was used to achieve higher accuracy.

The LAA takes up a small part of the entire CT volume. In order to boost performance, our approach requires the user to mark a bounding box which contains the LAA in all phases by selecting four fiducial points at the 45% phase. (Fig. 5 b–d show one of the first axial slice where the LAA appears. It also shows two of the middle axial slices where the area

where each pixel has to be assigned a label from the label set $L = \{0, 1\}$. Note that 0 and 1 represent the background and foreground, respectively. Let $x = \{x_1, \ldots, x_v, \ldots, x_{|\nu|}\}$ be a binary set that defines a segmentation on the image with $|\nu|$ equal to the number of pixels and each x_v is a label assigned to the corresponding pixel. Then the pixel set is divided into two subsets: pixels with label 0 and pixels with label 1. We formulate the labelling problem as a parametric energy minimization framework:

[1] We prefer 2-D slices to 3-D volume because we can parallelize the segmentation pool generation step which is the most time-consuming with 2-D slices processed independently. Axial slices are chosen because sagittal and coronal slices are no better for studying LAA morphology [1], while the number of slices in the axial plane is much less.

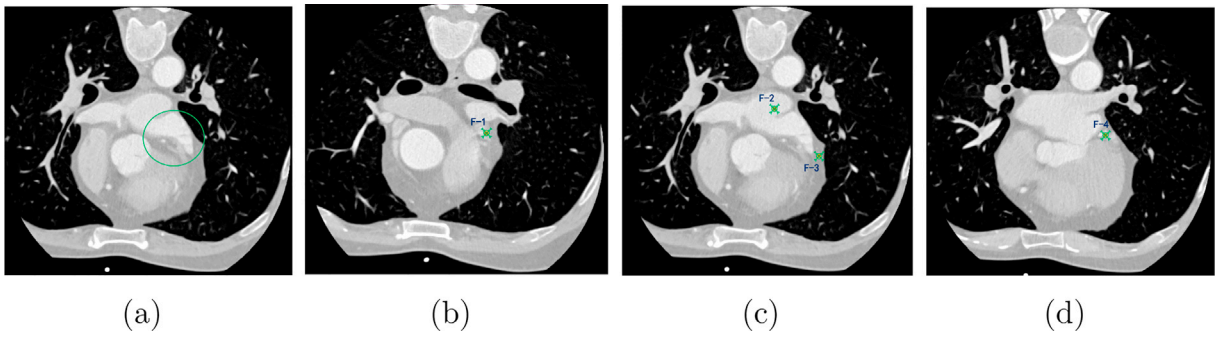

Fig. 5. The LAA and The ROI of LAA defined by four fiducial points. (a) The LAA marked by the circle. (b) One fiducial point on the initial axial slice where the LAA emerges. (c) Two fiducial points corresponding to diagonal corners of the maximal rectangle. The maximal rectangle encloses the LAA closely on the mid-axial slice in which the LAA area is normally the largest. (d) One fiducial point on the end of the axial slice where the LAA will ceases to exist.

Fig. 6. Seed hypothesis. Small magenta squares represent different foreground seeds placed in rectangular grid. Blue lines on image borders represent background seeds. We also propose a segmentation scheme for two different foreground seed assumptions. In each cluster. λ increases from left to right with the image nodes tend to foreground. (For interpretation of the references to color in this figure legend, the reader is referred to the Web version of this article.)

$$E^{\lambda}(x) = \sum_{u\in\nu} U_{\lambda}(x_u) + \sum_{u,v\in\varepsilon} B_{uv}(x_u, x_v). \tag{1}$$

In Eq. (1), $U_{\lambda}(x_u)$ is a unary term, $B_{uv}(x_u, x_v)$ is a binary term, and $\mathbf{x} = \{x_1, \cdots, x_u, \cdots, x_{|\nu|}\}$ is the former label set. $x_u \in \{0, 1\}$. 0 represents the background and 1 represents the foreground. $G = (\nu, \varepsilon)$ is an undirected graph with nodes ν and edges ε. Let $I(\nu) \rightarrow R^3$ represent an image defined on a set of pixels ν. Note that each node is a pixel of the image on the edges of the graph. $G = (\nu, \varepsilon)$ encodes the similarity between neighboring pixels. Unlike the traditional energy function in graph-cut, the unary term $U_{\lambda}(x_u)$ of our energy here is a monotonic non-decreasing function of λ in following conditions:

$$U_{\lambda}(x_u) = \begin{cases} 0 & \text{if } x_u = 1, u \notin \nu_b \\ \infty & \text{if } x_u = 1, u \in \nu_b \\ \infty & \text{if } x_u = 0, u \in \nu_f \\ f(x_u) + \lambda & \text{if } x_u = 0, u \notin \nu_f. \end{cases} \tag{2}$$

In Eq. (2), ν_b is the set of background seeds while ν_f is the set of foreground seeds. $f(x_u) + \lambda$ is a cost which is caused by assigning the non-foreground seed pixels to the background. It is a sum of two terms: a pixel-dependent term $f(x_u)$ and a uniform offset λ. We can use two different forms of $f(x_u)$ in practice. One is constant and equals 0. The other form uses intensity distribution. Specifically, the intensity distributions $p_f(u)$ and $p_b(u)$ are estimated respectively on the seed sets ν_f and ν_b. Then $f(x_u) = \ln p_f(u) - \ln p_b(u)$ is derived where $p_f(u) = \sum_k \pi_k \cdot N(I_u|\mu_k, \sigma_k)$ is the probability of pixel u belonging to the foreground and $p_b(u)$ has the similar form. Note that I_u is the grayscale value of pixel u. $N(I_u|\mu_k, \sigma_k)$ denotes the normal distribution of I_u with a mathematical expectation of u_k and a variance of σ_k. λ can change and as λ increases, the image nodes tend to be in the foreground due to the monotonicity of the function (Fig. 6). Therefore λ is called a foreground bias.

In addition, the binary terms are similar to traditional graph-cut:

$$B_{uv}(x_u, x_v) = \begin{cases} 0 & \text{if } x_u = x_v \\ A \cdot \exp\left(-\dfrac{(I_u - I_v)^2}{2\sigma^2}\right) \cdot \dfrac{1}{\mathrm{dist}(u, v)} & \text{if } x_u \neq x_v, \end{cases} \tag{3}$$

where A is the scaling factor and σ can be estimated as "camera noise" [12]. Note that we use an 8-neighborhood system in 2-D images, $\mathrm{dist}(u, v)$ is the distance of pixel u and pixel v. Finally, parametric max-flow is used to solve this energy minimization Eq. (1) with a set of λ values while the traditional max-flow method just solves the single λ problem. λ is changeable in this problem and it is why this approach is called "parametric" [15,23]. also discuss that the parametric max-flow is in the same complexity as the max-flow in graph-cut, which demonstrates that parametric max-flow is quite efficient.

3.1.2. Ranking and selection of proposals

Our goal is to select the proposals that largely overlap with the ground truth in each pool. Whereas the segmented image features can reflect the proposals' quality, one feasible approach is introducing a ranker to rank all proposals based on segmented image features and keeping the top one as the final selected result (Step 3 in Fig. 4). Specifically, the problem of ranking proposals are cast as regression based on the quality measure of proposals against their segmented image features.

Covering [24] is used as the quality measure for a set of segments concerning the ground truth, which is defined as:

$$\mathscr{C}(Q, Q'(r)) = \frac{1}{N}\sum_{R\in Q}\left|R\right| * \max_{R'\in Q'(r)} \mathscr{D}(R, R'), \tag{4}$$

where Q is the set of ground truth segments, Q' is the set of Auto segments and $Q'(r)$ is the subset of Auto segments at rank r or higher. N is the number of pixels belonging to annotated objects, R and R' represent the regions of ground truth and Auto segments respectively. $|R|$ is the number of pixels in the ground truth segment R, and $D(R, R')$ is a similarity measure between regions. **Dice Overlap** [25,26] is defined as:

$$\mathscr{D}(R, R') = \frac{2|R \cap R'|}{|R| + |R'|}. \tag{5}$$

It is the ratio of the intersection of regions to the average volume.

The regression is maximum similarity $\max_{R\in Q} D(R, R')$. Random forests [27] are adopted in the regression for ranking. In random forests, the number of trees is 120, the number of candidate variables randomly selected from each split node is set to 6, and other parameters are default.

Two kinds of features are used to describe each proposal: the mask features and the Gestalt features. Mask features encode the statistics of the position, scale, and shape of the segmented region. They consist of 17 features in total, including the relative position of the image center $((Cent_{\text{box}} - Cent_{\text{img}})/width_{\text{img}}$ and $(Cent_{\text{box}} - Cent_{\text{img}})/hight_{\text{img}}$, here, $Cent_{\text{box}}$ is the centriod of boundingbox, $Cent_{\text{img}}$ is the centriod of image), the relative area to the image area ($Area_{\text{box}}/Area_{\text{img}}$), the lengths of the major and minor axis of the ellipse that has the same normalized second central moment as the region, the relative distance between the extreme points in the region and the image center to the image size, ratio of pixels in the region to pixels in the bounding box tightly containing the region, proportion of the pixels in the convex hull that are also in the region, and Euler number(Euler number of the bounding box). These features can be conveniently computed invoking the **regionprops** function in **Matlab**. Gestalt psychology [28] argues that our vision system tends to group similar small parts as a whole when we try to understand an image. Gestalt features are rather important for visual grouping. They are mid-level cues encoding data such as the similarity and consistency properties of an object. In our paper, the Gestalt features consist of six features, including the histogram of the foreground region, relative intra-region edge energy which is the sum of inner edge energy of the foreground region divided by the total of foreground pixels, relative inter-region edge energy which is the sum of the edge energy along the boundary divided by the boundary length (the edge energy is computed using **globalPb** [24]), and the boundary curvature (an angle approximation is used to the curvature on three adjacent points of the boundary [29], which regularly sampled with every 18 pixels). All 23 features are normalized by subtracting their mean values and dividing by their standard deviation. Finally, from the analysis of the significance of the features learned by the random forests regression, we found that the borderline and contextual properties are much stronger than the ones of regions. λ tends to be a very small value close to 0.

3.1.3. 3-D model building using spatial continuity

After picking out the best proposal for each slice, we can merge all the selected 2-D proposals into a 3-D model. However, the continuity and consistency between adjacent slices are ignored while they are useful for improving the quality of the 3-D model. In object tracking, time continuity represents a strong correlation between adjacent frames and a very important cue. Similarly, in our task, the segmentation results of the adjacent slices are strongly related to each other, which we call spatial continuity. Spatial continuity can assist in recovering the 3-D model more easily. Additionally, we consider three adjacent slices. For the current slice, we check the segmentation results of its former and latter slices to recover the missing disconnected components of the LAA and correct the small leakage to the neighboring anatomical structures.

3.2. Multi-phase LAA segmentation

A preliminary single phase LAA segmentation has been reported [16]. However, LAA is a flexible organ in reciprocating motion. Single phase segmentation is only the beginning of the study of LAA. To accurately grasp its structure and functions, our group has to perform multi-phase segmentation in the entire cardiac cycle continuously.

After segmenting the 45% phase, we would use this segmentation result to generate the initial seed points for its adjacent phases. In general, the foreground seed points are generated according to Eq. (6):

$$\boldsymbol{S}_{i\pm1} = \text{Erosion}(\boldsymbol{M}_i \& \text{Thresh}(\boldsymbol{I}_{i\pm1})), \tag{6}$$

where M_i is the segmentation mask of a prior segmented image, $I_{i\pm1}$ is the adjacent image and $S_{i\pm1}$ is the initial seed point for the adjacent image. Whereas the intensity of the blood pool is typically over 250HU, we set a threshold of the image before the "*and*" operation with a segmented mask. After the "*and*" operation, erosion is performed on the result, in the case there are some small false foreground seeds. The erosion mask used in our experiment is $5 \times 5 \times 5$ matrix of all 1. The foreground seeds generation approach is accurate, efficient and sufficient because we take advantage of following fact:

- A typical CT examination just requires a few minutes and the patient almost lays still during a quick examination. Thus, the position of the LAA in the image of the entire cardiac cycle almost does not change, but the size of the adjacent LAA also changes a little. This renders our foreground seed accurate.
- The 45% phase has the biggest LAA volume and the 95% − 5% phase has the smallest volume according to [22]. The multi-phase segmentation procedure is performed forward from 45% to 5% and backward from 45% to 95%,

5%← 10%← 15%← 20%← 25%← 30%← 35%← 40%← 45%, 45% →50% →55% →60% →65% →70% →75% →80% →85% →90%→95%.

- Therefore, the segmentation mask is conducted from the bigger phase to smaller phase, which will generate sufficient foreground seed points.

For background seed points, we simply use the set of pixels that cover the right and top image borders. Given the sufficiently generated image seed points, we use a graph-cut approach to segment the adjacent image $I_{i\pm1}$. Similar to Eq. (1), the energy function of graph-cut is defined as follows:

$$E(x) = \lambda\sum_{u\in\nu} U(x_u) + \sum_{u,v\in\varepsilon} B_{uv}(x_u, x_v), \tag{7}$$

where λ is a user specified value to balance the unary term and binary term. λ is 0.02 in Eq (7) based on the following consideration [12]: the region of interest (ROI) is determined by random users and cannot be predicted. The segmentation algorithm in practice can not rely on any particular region attribute. Moreover, most objects of interest are divided along high contrast boundaries in the image. We actively adopt boundary items with discontinuous penalties. Strong constraints as the inputs of seeds can bring "high-level" contextual reference. Consequently, λ should be a small value greater than 0 (refer to the last paragraph of Section 3.1.2). The unary term is defined as follows:

$$U(x_u) = -\ln p(I_u|x_u), \tag{8}$$

where, I_u is the grayscale value of pixel u. $U(x_u)$ is related to the probability that the pixel u belongs to the foreground or background with respect to $x_u = 1$ or $x_u = 0$. The binary term is the same in Eq. (3). The

max-flow/min-cut solver is used to calculate the segmentation result. By performing the above process iteratively, we finally segment all of the image sequences accurately and rapidly.

Algorithm 1 Limit threshold minimization

Step 1 Find the minimal gray threshold in $\Delta S^{\text{Squeeze}}$. denoted by $\text{mgt} = \min\{G_\sigma * I|(x,y) \in \Delta S^{\text{Squeeze}}\}$;

Step 2 Set t=0;
Computer $\Delta S_t^{\text{Squeeze}} = \{(x,y) \in \Delta S^{\text{Squeeze}}|G_\sigma * I \geq (mgt + t)\}$;
Computer $S_{(n+1)}^{\text{separate}} = S_{n+1}^{\text{Squeeze}} - \Delta S_t^{\text{Squeeze}}$;
While The parts of the largest connected domian in $S_{(n+1)}^{\text{separate}}$ and S_n^{Final} have a significant difference.
t=t+1;
Compute $\Delta S_t^{\text{Squeeze}}$ and $S_{(n+1)}^{\text{separate}}$;
EndWhile;

Step 3 Remainder the largest connected domains of $S_{(n+1)}^{\text{separate}}$ as the segregative result.

In the segmentation of the biggest volume phase, we leverage spatial continuity to improve the quality of our final result. Here a similar property is also used, which is the temporal continuity of the adjacent phases' segmentation results, to correct some errors in the multi-phase segmentation. For example, because the LAA is constantly moving and deforming, its lobes occasionally overlap. Sometimes the segmentation result tends to obtain wrong number of lobes. By cross-checking the segmentation results of adjacent phases, these problems are avoided. Due to the relatively low grayscale of the narrow squeezed area of the lobes compared to other adjacent regions, we present the cross-checking of the segmentation results of adjacent phases, named limit threshold minimization(LTM). In the algorithm of LTM, S_n^{Final} is defined as the space region inside the segmentation result of the nth phase, and the lobes of LAA are not squeezed in S_n^{Final}. Suppose some lobes are squeezed in the $(n+1)$th phase, and the space region inside the contour of segmentation result is defined as $S_{n+1}^{\text{Squeeze}} = \{(x,y) \in \Phi\}$. An obvious difference exists between the maximally connected domains of S_n^{Final} and S_{n+1}^{Squeeze}. Thus, it is easy to judge the connectivity of the LAA in the $(n+1)$th phase using the segmentation results of the nth phase. We define the space region $\Delta S^{\text{Squeeze}}$ as:

$$\Delta S^{\text{Squeeze}} = S_{n+1}^{\text{Squeeze}} - S_{n+1}^{\text{Squeeze}} \cap S_n^{\text{Final}}. \tag{9}$$

Note that $\Delta S^{\text{Squeeze}} \subseteq S_{n+1}^{\text{Squeeze}}$. Obviously, the cutting line between the two lobles is located in $\Delta S^{\text{Squeeze}}$. Using the marked contrasts between $\Delta S^{\text{Squeeze}}$ and the surrounding LAA tissue, the approach of LTM is detailed in Algorithm 1.

4. Volume calculation to assist the AF diagnosis

There is a positive correlation between LAA volume and AF risk. Vaziri SM *et al* [30]. showed a 39% increase in the risk of AF with a 2 mm^3 increase in the LAA volume. Therefore, we propose an algorithm of the voxel summing in a 3-D segmented object to calculate the LAA volume. Furthermore, the "volume-phase" curve is generated and the key functional metrics are obtained.

4.1. Detection of the ostium of LAA

In the functional analysis of LAA, we need to accurately calculate the volume of LAA and find the boundary between LAA and LA, which is the ostium of LAA. Along this boundary, we separate LAA from LA. This is because the segmentation of the LAA is performed in a bounding box (Section iii. A), and the segmentation result includes a portion of the LA (left atrium), although the lobes of LAA are well-segmented.

There is a large surface curvature change in the transitional region between the LA and LAA. Therefore, we propose a self-adaptive method based on optimization to find a smooth closed boundary of the highest curvature, which is the ostium of the LAA neck [5]. The specific method is as follows.

The standard coordinate system is based on the short-axis slice plane of the CT as the X-Y plane, a corner point of the initial slice as the coordinate origin, and then the right-hand rule to establish the Z-axis direction. In this coordinate system, the mean value of the Z-axis coordinates of all the points belonging to the LAA model is first calculated to determine the height h. Further, a plane parallel to the X-Y plane is determined at height h, which plane intersects the surface model of the LAA and all intersection points form the proximal ring of the LAA. The ring is interpolated with cubic spline [31], and densely resampled at the points with a fine resolution (e.g. 0.2 mm, this distance is less than the voxel unit). We search for a point, which is nearest to all points of the ring in terms of Euclidean distance. This point is called the centroid O, that is:

$$\sum \text{dist}(R, O) \rightarrow \text{MIN}, \tag{10}$$

where R is a point on the ring, O is the centroid of the ring. The normal direction N of the ring parallel to the Z axis through the O. Then a plane perpendicular to the ring is determined, which passes through R_i (a point on the ring) and O. The plane rotates around the axis which is the normal vector N passing O. The intersections of the series of rotating planes with the LAA surface are the set of contour lines of the LAA, $c_n = \{c_i, i = 0, 1, 2, \cdots, n-1\}$. as shown by the dotted lines in Fig. 7 (a). We constrain the longitudinal size of the contours to 31 mm (the length of transitional region between the LA and LAA is about 20–30 mm anatomically). Before solving the curvature, the digital curve was interpolated with cubic spline [31] satisfying C2 continuity condition, and the digital curve was densely resampled at the points with a fine resolution (e.g., 0.2 mm, this distance is less than the voxel unit). The interval between adjacent pixels is a constant, so as to obtain the continuous edges based on the digitized curve. This interpolation calculation is simple, and can achieve satisfactory numerical results with reducing the noise interference and irregularity of contours. If the contour is represented by the vector $\mathbf{v}(l)$ ($\mathbf{v}(l) = (x(l), y(l), z(l))$, which are interpreted as points), l is the arc length as parameter [32], the following approximations are used [29]:

$$\left|\frac{d\mathbf{v}_i^{J(i)}}{Dl}\right| \approx \left|\mathbf{v}_i^{J(i)} - \mathbf{v}_i^{J(i-1)}\right|, \tag{11}$$

where $\mathbf{v}_i^{J(i)}$ is the vector of corresponding points $S_i^{J(i)}$, these points are evenly spaced at unit intervals. Furthermore, the curvature of a point $S_i^{J(i)}$ from the contour c_i (Fig. 7) is defined as:

$$C\left(S_i^{J(i)}\right) = \left|\frac{d^2\mathbf{v}_i^{J(i)}}{Dl^2}\right| \approx \left\|\left(\mathbf{v}_i^{J(i+1)} - \mathbf{v}_i^{J(i)}\right) - \left(\mathbf{v}_i^{J(i)} - \mathbf{v}_i^{J(i-1)}\right)\right\|. \tag{12}$$

And then calculate the maximum sum of curvature of all sampling points on every contour line.

$$E = \left(S_0^{J(0)}, \cdots, S_{n-1}^{J(n-1)}\right) = \arg \max_{J(0),\cdots,J(n-1)} \sum_{i=0}^{n-1} C\left(S_i^{J(i)}\right), \tag{13}$$

where, $S_i^{J(i)}$ indicates the jth point on the ith contour line and $S_i^0 = R_i$. $C(S_i^{J(i)})$ is the curvature at point $S_i^{J(i)}$.

When we calculate the curvature using differential geometry, the second order derivatives of the contour line need to be obtained, and the calculated curvature sometimes tilts in the wrong direction. The final boundary may be located far away from the LAA ostium in some data. Therefore, in order to improve robustness, we add a bias, $\left|\left|N \cdot (S_i^{J(i)} - S_i^0)\right|\right|$, which is the 2-norm of the inner product of N and $(S_i^{J(i)} - S_i^0)$, to pull the boundary toward the LAA ostium, N is the normal vector of the ring. To ensure the smoothness of the boundary, we require the difference between J_i and $J_{(i+1)}$ from the adjacent sampling point to be less

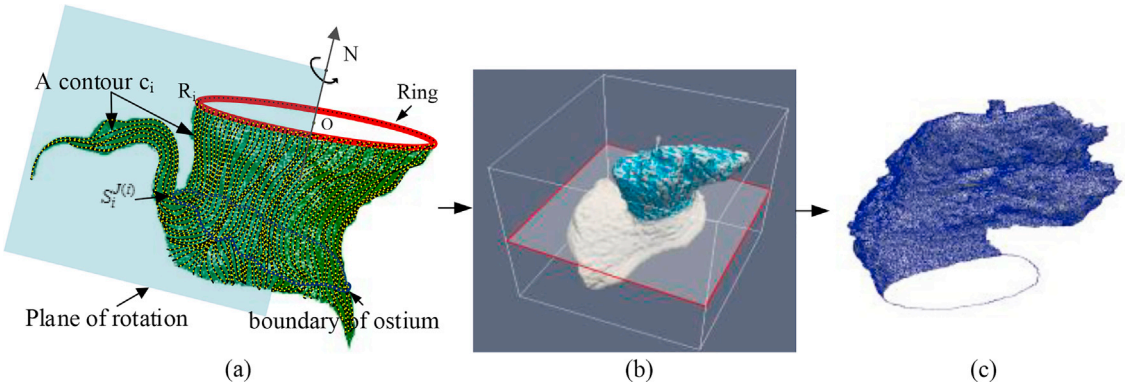

Fig. 7. Removing the part of LA from the LAA. (a) The ostium of the LAA neck obtained by calculation of curvature, the corresponding boundary is marked by the blue line. (b) The initial surface modle of the LAA. (c) The obtained result, which is a entire LAA. (For interpretation of the references to color in this figure legend, the reader is referred to the Web version of this article.)

than 1. Similarly, to ensure the boundary is closed, we require the difference between J_0 and $J_{(n-1)}$ from the start and end point to be less than 1.

$$|J(i) - J(i+1)| \leq 1. \tag{14}$$

$$|J(n-1) - J(0)| \leq 1. \tag{15}$$

To satisfy constraint (15), we construct the following item to the objective function, $e^{\frac{i-I_{\max}}{N_0}} \cdot \frac{1}{(J(i)-J(0))^2+\varepsilon}$. Hence the final objective function is

$$\max \sum_{i=0}^{n-1} \left[C\left(S_i^{J(i)}\right) + w_1 \left\| N \cdot \left(S_i^{J(i)} - S_i^0\right) \right\| + w_2 e^{\frac{i-I_{\max}}{N_0}} \cdot \frac{1}{\left(J(i) - J(0)\right)^2 + \varepsilon} \right], \tag{16}$$

where $I_{\max} = n-1$, is total number of contour lines. N_0 is step parameter, the weight of adjusting the step length. J(0) is the number of initial point. ε is a longitudinal offset parameter that adjusts the offset cost. The default values of the parameters are $N_0 = 5$, $\varepsilon = 0.001 w_1 = 0.002$, $w_2 = 1$ respectively.

The optimization problem is solved by a dynamic programming algorithm from step $i = 0$ to $i = n-1$. At the ith step, $J(i)$ is solved by the following optimization model

$$J(i) = \arg \max_{|J(i)-J(i+1)|\leq 1} C\left(S_i^{J(i)}\right) + w_1 \left\| N \cdot \left(S_i^{J(i)} - S_i^0\right) \right\| + w_2 e^{\frac{i-I_{\max}}{N_0}} \cdot \frac{1}{\left(J(i) - J(0)\right)^2 + \varepsilon}. \tag{17}$$

A boundary (the blue line in Fig. 7 (a)) is obtained by the dynamic programming algorithm, which is the ostium of the LAA neck. An entire LAA is successfully obtained (Fig. 7 (c)).

4.2. Volume calculation methods

The calculation volume of LAA can not only quantitatively evaluate the size of the LAA, but also indirectly reflects the function of LAA to diagnose AF [33,34]. We propose an integral based method for calculating the LAA volume [35]. The voxel summing approach in a 3-D segmented object is used to calculate the area S by traversal accumulation of the voxels in the target region of each slice, and then the volume of the target object is obtained:

$$V = \sum_{i=1}^{N-I} \frac{\left(S_i + S_{i+1} + \sqrt{S_i S_{i+1}} \times h\right)}{3}, \tag{18}$$

where N is the number of slices, h is the spacing between the two adjacent slices. This integral process is simple and efficient, while the voxels are not virtually isotropic. The scanned CT information contains the Element Spacing (0.357422 mm, 0.357422 mm, 0.449951 mm) and Dim Size (512 × 512). The spacing between slices is not equal to the spacing of voxels within the slices. The size of h affects the accuracy of the volume calculation. The volume of LAA is small, only 0.7–19.2 ml [36]. Hence the thickness of the slice has to be thin. The LAA volume consists of 60–80 axial slices, which can meet the precision requirement of calculating its volume.

4.3. Calculation of function metrics based on the "volume-phase" curve

There are twenty phases in each cardiac cycle. We calculate the volume of LAA at each phase and then plot the "volume-phase" curve in detail to analyze the pattern of LAA movement and deformation. Finally, several LAA function metrics are calculated: the left atrial appendage ejection fraction (LAA-EF), left atrial appendage peak emptying flux (LAA-PEF) and left atrial appendage peak filling flux (LAA-PFF). These metrics are the independent risk factors of left atrial appendage thrombus (LAAT) [37–39].

4.3.1. LAA-EF

In previous studies, the LAA-EF was calculated by the area of an ultrasound image [40]. However, because of the image shift, it is easy to produce some errors. We use the volume to replace the area for calculation.

$$\text{LAA} - \text{EF} = \frac{\text{LAA} - \text{V}^o_{max} - \text{LAA} - \text{V}^o_{min}}{\text{LAA} - \text{V}^o_{max}} \times 100\%, \tag{19}$$

where $\text{LAA} - \text{V}^o_{max}$ represents the maximal volume of LAA in a entire cardiac cycle, $\text{LAA} - \text{V}^o_{min}$ represents the minimal volume of LAA in a entire cardiac cycle.

4.3.2. LAA-PEF and LAA-PFF

LAA-PEF and LAA-PFF can directly reflect the systolic and diastolic rates of LAA. A retrospective ECG gating technique is used to estimate the time.

In the descending part of the "volume-phase" curve, we have:

$$\text{LAA} - \text{PEF} = \frac{\text{LAA} - \text{V}^e_{max} - \text{LAA} - \text{V}^e_{min}}{t}, \tag{20}$$

where $\text{LAA} - \text{V}^e_{max}$ represents the maximal volume of LAA in emptying stage of a entire cardiac cycle, $\text{LAA} - \text{V}^e_{min}$ represents the minimal volume of LAA in emptying stage of a entire cardiac cycle. In a cardiac cycle, the movement of LAA consists of 4 stages: filling, emptying, re-filling, and re-

emptying.

Similarly, in the rising part of the "volume-phase" curve, we have:

$$\mathrm{LAA-PFF}=\frac{\left|\mathrm{LAA}-\mathrm{V}_{min}^{f}-\mathrm{LAA}-\mathrm{V}_{max}^{f}\right|}{t}, \tag{21}$$

where $\mathrm{LAA}-\mathrm{V}_{max}^{f}$ represents the maximal volume of LAA in filling stage of a entire cardiac cycle, $\mathrm{LAA}-\mathrm{V}_{min}^{f}$ represents the minimal volume of LAA in filling stage of a entire cardiac cycle.

5. Experiments and results

5.1. Dataset

We collected 100 sets of coronary CTA data with ECG examination, scanned by Philip 256-iCT from June 2016 to July 2017. In the LAA segmentation, we use 50 cases as the training set, and the remaining 50 cases as the test set. In the computer-aided diagnosis of AF, 55 cases are used for training, and the remaining 45 cases are used for testing. In these CT data, each cardiac cycle contains 20 phases; each volume contains about 500 slices; each slice has 512×512 pixels with an isotropic resolution of about 0.36 mm. The slice thickness is 0.44 mm for each volume. The time resolution of the 4D-CT satisfies the requirement to calculate volume change ratio of the LAA in single cardiac cycle. Note that the patients with AF have large individual differences in heartbeat, a retrospective ECG gating technique is used to estimate the time in calculation the LAA-EF, LAA-PEF and LAA-PFF of each patient in practice. For a comprehensive analysis, we divide these patients into three groups according to the clinical diagnosis: 22 cases of no detected atrial fibrillation (NAF), 49 cases of paroxysmal atrial fibrillation (PAF), and 29 cases of chronic atrial fibrillation (CAF). Then, the patients with AF are divided into two groups: 21 cases with LAAT (LAA thrombi, filling defect of contrast agent on CT) and 57 cases without LAAT.

5.2. Ground truth

With the assistance of two experienced radiologists and a cardiologist, we obtained the initial ground truth using a paintbrush tool in 3-D SLICER 4.4 slice by slice at the voxel level on 100 sets of CT data. For the manual method, the segmentation results of single phase are morphologically credible. However, the manual methods do not adequately exploit the continuity features of the entire cardiac cycle. The parts of folding and squeezing in LAA cannot be separated well. To ensure the accuracy of ground truth, we adopted the strategy similar to the last paragraph of Section 3.2 for post-processing. Based on the segmentation results of multi-phase, the final ground truth was obtained by using the cross-validation of adjacent phases. Further, the technicians manually measured the shape and size of LAA with the corresponding 3-D CT model.

5.3. Accuracy of multi-phase segmentation results

We analyze the accuracy by comparing the results of automatic segmentation and ground truth. It includes two aspects: one is a similarity analysis based on volume measurement and the other is an error analysis based on surface distance measurement.

5.3.1. Similarity results

The similarity can be measured by calculating the Volume Overlap (VO) ratio and Dice Coefficient (DC) ratio. These two ratios are calculated as follows:

$$VO=\frac{\left|V_{seg}\cap V_{gd}\right|}{\left|V_{seg}\cup V_{gd}\right|}, \tag{22}$$

$$DC=\frac{2\left|V_{seg}\cap V_{gd}\right|}{\left|V_{seg}\right|+\left|V_{gd}\right|}, \tag{23}$$

where V_{gd} , V_{seg} denote the volume of the ground truth and the automatic segmentation respectively.

Fig. 8 lists the calculation results of the average VO and DC for the test sets of 50 cases, which demonstrate that the automatic segmentation results of LAA exhibit a high degree of similarity to ground truth in the entire cardiac cycle. But from the comparison results, the similarities from some phases are slightly lower and the variances are mildly larger. The reasons are that the LAA is beating rhythmically in the entire cardiac cycle. When filling, the volume increases and the endocardiac folds decrease, resulting in the better segmentation effects. When emptying, the volume decreases, the endocardiac folds increase, and the caeca of the LAA (the lobes of the LAA) would be squeezed with each other, resulting in the weaker segmentation effects. The LAA has a variety of morphology which can be divided into chicken wing, wind sock, cauliflower and cactus etc. [41]. The segmenting effects are relatively satisfactory for the LAAs with large volume and simple structure. In addition, as the motion artifacts occur or the contrast agent is not fully filled into the LAA when the CT image is acquired, a few LAAs are difficult to achieve satisfactory segmentation using manual or automatic methods.

5.3.2. Error results

Surface distance measurement is used to measure the minimum distance from each point of the surface of the automatic segmentation model to ground truth. This approach can evaluate the accuracy of the automatic segmentation result intuitively. The distance is calculated by Refs. [42,43]:

$$d_i=\min\left(\left|X_{\mathrm{gd}i}-X_{\mathrm{seg}i}\right|\right), \tag{24}$$

where, $X_{\mathrm{gd}i}$ is the closest point on ground truth to the point $X_{\mathrm{seg}i}$ on the automatic segmentation model, and the same point may be calculated several times, d_i is the distance between two points $X_{\mathrm{gd}i}$ and $X_{\mathrm{seg}i}$. This evaluation function reflects the degree of overlap between ground truth and automatic segmentation results.

Fig. 9 shows one example of the error distribution of the points around LAA surface. The segmentation errors are below 1 mm in most areas. However, in some areas, the segmentation accuracy declines slightly, such as the transition zone lying between the left atrium (LA) and LAA. The reason is the boundaries selected for ground truth based on manual segmentation differ from those for automatic segmentation. Note that manual segmentation is single-phase image processing, while our approach takes into consideration the morphological changes of LAA and the topological relationship between adjacent phases. The difference between manual and automatic segmentation does not necessarily mean an "error". To obtain the ground truth of the entire cardiac cycle, the results of manual segmentation were ameliorated in the first paragraph of Section 5.2.

Fig. 10 shows the Box and Whisker plot for the average relative errors of the surface distance at different phases in the test sets of 50 cases. It can be observed that the average segmentation errors are very concentrated in 15% to 85% and most of them are below 2%, which demonstrates the robustness of this approach. However, the errors of some samples are high at the 5%, 10%, 90% and 95% phases, but they are less than 5% mostly. The relative error is dispersive at the beginning and the end of entire cardiac cycle, which is mainly due to the weaknesses of CT imaging (the LAAs in these phases are small in size, with loose folds and complex structure). However, these images are also difficult for manual segmentation.

5.4. Advantages of multi-phase segmentation

The serial segmentation of all phases for one set of scan data takes about 10 min on an Intel *i*7 CPU @ 2.8G Hz with 8 GB RAM. Far faster

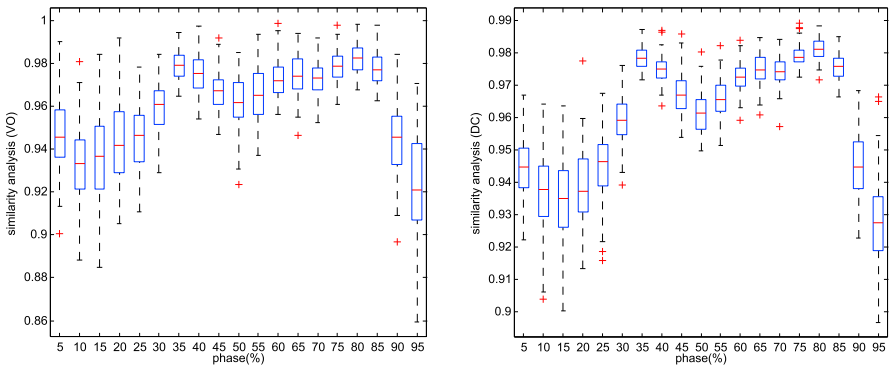

(a) (b)

Fig. 8. The Box and Whisker displaying the similarity analysis of volume measurement. (a) Volume Overlap (VO) ratio. (b) Dice Coefficient (DC) ratio.

than the manual segmentation time for which experienced clinicians will employ about 4 h.

We take full advantage of the temporal dimension information in multi-phase segmentation. Compared with the single-phase independent segmentation algorithm, the advantages of our approach are as follows:

- According to the facts that the LAA morphological changes are continuous, the cross-checking of multi-phase models is carried out. We successfully remove self interferences which are shrinkage deformation and the overlapping extrusion of the self-organized unit. These interferences seem to fuse together in the gray image, as shown in Fig. 11;
- Successfully removing the neighboring interference such as tissues and vessels. Given that CT is tomographic, gray patches of LAA and blood vessels are irregular, fragmented in some slices, which are not easy to separate based on a single slice or single phase, and our approach solves this problem, as shown in Fig. 12.

5.4.1. *Removal of the self interferences*

The LAA is constantly moving and deforming, and its lobes occasionally overlap. Sometimes the segmentation result tends to obtain the wrong number of lobes. By cross-checking the segmentation results of adjacent phases, these problems are avoided, as shown in Fig. 11.

After a single phase separation (Fig. 11 b), the model shows that its tip is the entire lobe, with a concave groove on the lobe instead of a crack. After comparing and judging by multi-phase (Fig. 11 a), we find that this is because the two lobes are squeezed too tightly at the moment and cannot be distinguished correctly on the CT image. Our approaches can separate the two lobes through the groove automatically. From different points of view, the corrected 3-D model are shown in Fig. 11 c.

5.4.2. *Removal of the neighboring interferences*

In term of anatomical structure, the LAA is adjacent to the left superior pulmonary vein (LSPV), and the ridge between the two tends to be misclassified as the LAA. The LAA overlaps some parts of the left circumflex branch (LCX). It is difficult to distinguish LCX from LAA in some CT slices, as shown in Fig. 12 a, b. But these neighboring interferences do not occur in most of phases (Fig. 12 c).

In the multi-Phase LAA Segmentation, we would use the segmentation result of previous phase to generate the initial foreground and background seed points for its adjacent phases and the correlation of adjacent phases is enhanced, so that these neighboring interferences are removed to some extent. To make the segmentation approach more robust, a cross-validation strategy based on segmentation results of adjacent phases is used, as similarly detailed in the last paragraph Section 3.2. Hence, the rough model (Fig. 12 d) is compared and evaluated with multi-phase (Fig. 12 c), the LSPV and LCX are removed from the 3-D model, the end result is obtained (Fig. 12 e).

5.5. *Generation of the "volume-phase" curve*

The primary application of multi-phase LAA segmentation is to study the pattern of volumetric change of LAA in a cardiac cycle. After the volumes of 100 LAAs are calculated (Table 1), we develop the "volume-phase" curve and calculate the key functional metrics based on LAA volume to assist in the diagnosis of AF.

We generate a "volume - phase" curve based on the results of multi-phase segmentation. In the measurement of LAA function metrics, the LAA volume (Fig. 13 b)measurement replaces the previous area (Fig. 13 a) measurement to reflect the static or dynamic situation of LAA. In order to measure the accuracy of the "volume-phase" curve, we plot the "max slice area - phase" (Fig. 14 a) - similar to ultrasonography.

The "volume-phase"(Fig. 14 b) rises, descends and rises, descends again. It confirms that the LAA undergoes filling, emptying and re-filling, re-emptying in the entire cardiac cycle. The LAA can not only actively deform, but also passively shake. The origin of the passive shake is from the left ventricle (LV). Inside the ventricle, LV has a diastolic suction force to the LAA. Outside of the ventricle, the tension is generated by external collision (Fig. 1 a). This is the reason why the flux of filling is generally less than the flux of emptying. 45% phase reaches the peak of curve, 5% phase falls into the trough of curve, which proves that 45% phase is LAA end-diastole with the largest volume; 5% phase is LAA end-systole with the smallest volume. In 65% - 85% phase, the fluctuation range of the curve is relatively small, and the LAA is in self-slow elastic retraction. The LAA volume changes little and is close to the natural state. During this period, the parameters of LAA volume, ostium diameter and area are closer to the true value. These parameters are important for planning LAA occlusion [44].

5.6. *Calculation of key function metrics by "volume-phase" curve*

We calculate PFF, PEF and EF in each stage of a cardiac cycle of LAA by single maximal slice area and volume respectively on 100 sets of data (Fig. 15). There is a reasonable correlation between the "Area" method and "Volume" method for LAA-EF and LAA-PEF of patients with AF ($r = 0.96$, respectively, $p < 0.001$). The results of the "Max slice area" method will be affected by the uncertainty of the slice position, and it only depicts the LAA deformation of the direction parallel to the slice. In addition, the LAA movement is very complex. This maximum and minimum cross-sectional area of the LAA is affected by the contraction and diastolic movement of the heart and its own, resulting in the two not coming from the identical two-dimensional plane occasionally. However, it is a frequently-used approach taken by ultrasonography in clinical medicine. In the "volume" method, its spatial resolution and temporal resolution is high, the moving pattern of 3-D LAA is completely demonstrated within the entire cardiac cycle, from the ostium to caeca (the lobes of LAA). LAA volumetric parameters are more reliable (e.g. The EF measured by the volume has a better correlation with the PEF), which is superior to the

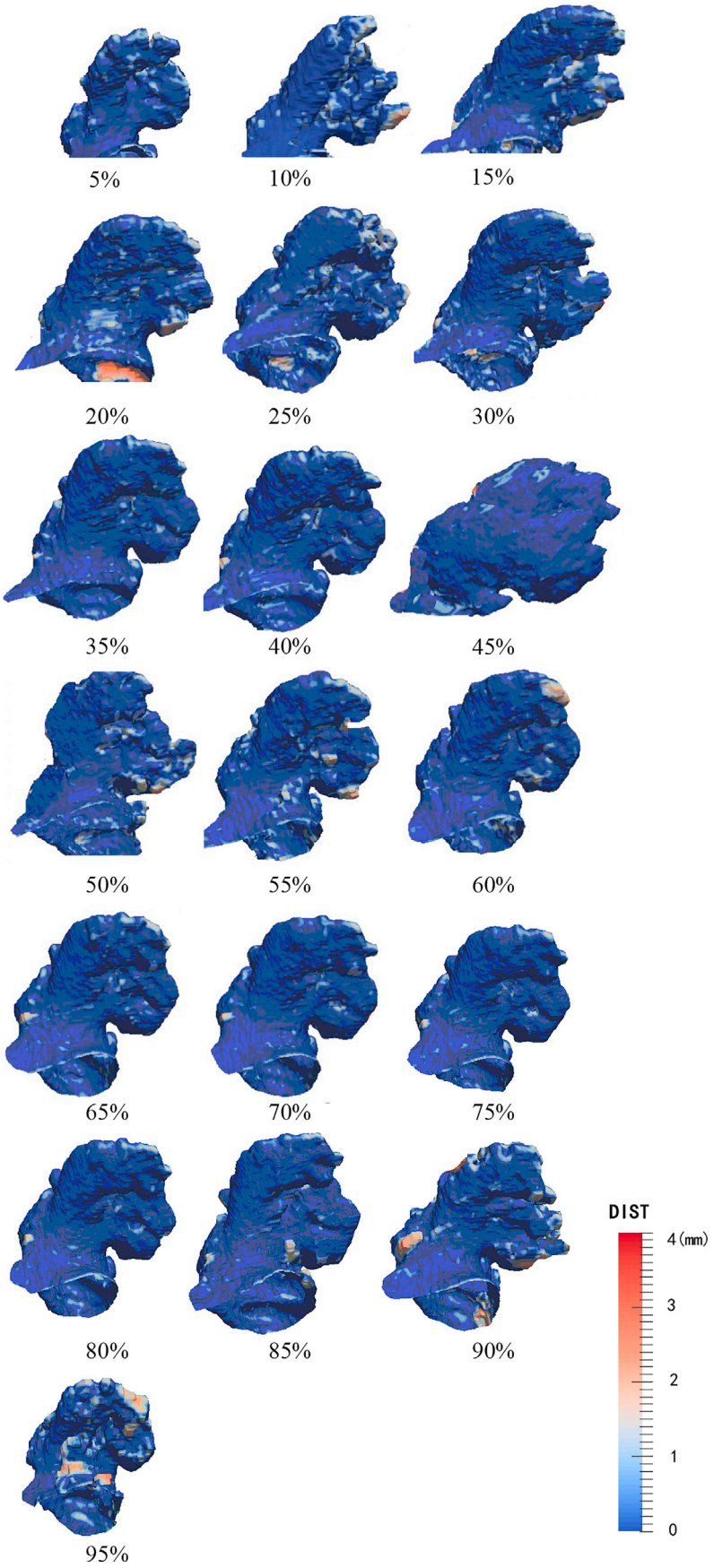

Fig. 9. The distribution of surface distance error of LAA at 5%-95% phases in the entire cardiac cycle. The color intensity is proportional to the error size. Relative to other parts, the errors increases in the ostium and lobes of the LAA. (For interpretation of the references to color in this figure legend, the reader is referred to the Web version of this article.)

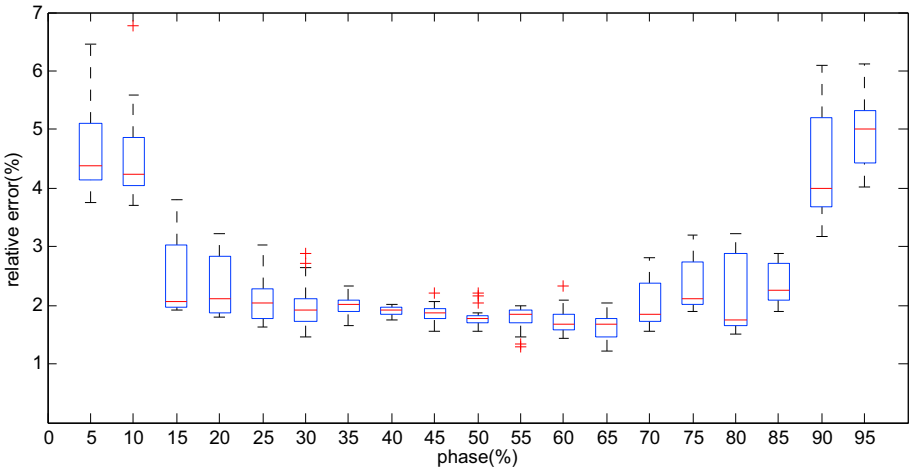

Fig. 10. The Box and Whisker displaying the relative errors of the surface distance between each phase.

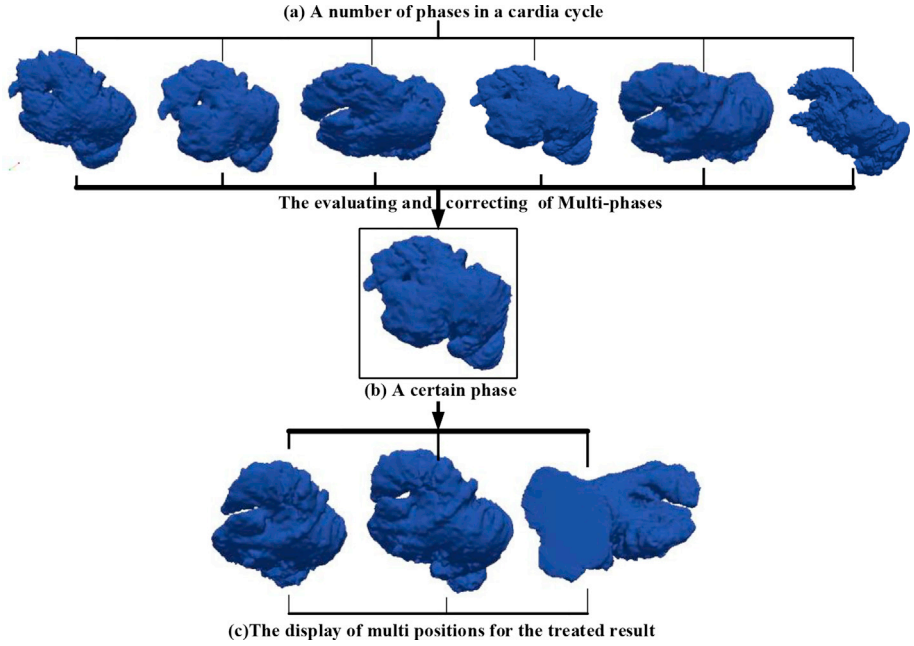

Fig. 11. Removal of self interferences by multi-phase assisting segmentation using LTM. The initial segmentation result (b) is evaluated and corrected by the multi-phase continuity (a), and the final result (c) is obtained.

conventional two-dimensional area method and has been used to evaluate the mechanical functions of LAA based on real-time three-dimensional transesophageal echocardiography (RT3D-TEE) [45].

5.6.1. Assisted diagnosis of AF using the multi-category SVMs classifier

We apply the multi-category SVMs [47] to achieve a computer-aided diagnosis of AF. Similar methods can be used to diagnose AF in ECG. Our data is divided into 3 groups according to the cardiac rhythm: NAF, PAF and CAF [48]. They have 7 main features based on volume as follows: The volume's mean and variance in volume-phase curve, 2 LAA-PFF, 2 LAA-PEF, 1 LAA-EF (Table 6). Due to the difference of dimensionality and numerical value of these characteristic parameters, the zero-one normalization is adopted to ensure that the data sequence involved in the analysis is basically in the same order of magnitude and realize dimensionless,

$$Y_i(k) = \frac{x_i(k) - \min x_i(k)}{\max x_i(k) - \min x_i(k)}, \qquad i = 0, 1, 3; \quad k = 1, 2, \cdots, 7. \tag{25}$$

where $x_i(k)$ is an initial characteristic parameter, and $Y_i(k)$ is corresponding normalized value. According to one-versus-one (OVO) in pairs [49,50], 3 bipartition SVMs are adopted between each other (NAF, PAF), (PAF, CAF) and (NAF, CAF) of 3 categories. 3 SVMs are trained independently in 55 sets of training samples (Table 2), and to construct the corresponding decision function. During the training process, each SVM penalty factor $C = 1$, each kernel is the radial basis function:

$$K(X, Y) = \exp\left(\frac{-\|X - Y\|}{2\sigma^2}\right), \tag{26}$$

where the radial basis parameter $\sigma = 1$.

The 45 sets of testing samples shown in Table 3 are categorized by using the trained 3 bipartition SVMs respectively. The final decision was based on the voting strategy, Max (vote(NAF), vote(PAF), vote(CAF)) to obtain the final diagnostic results of each sample on the test sets. The diagnostic accuracy compared with the original diagnosis of these cases in 45 testing is 93%. The reason for some errors is that sometimes CAF and PAF can be mistaken for each other because of the limited CT scan time. e.g. 2 cases of PAF are misclassified into CAFs, and 1 case of CAF is misclassified into PAFs in the testing sets. However, the proposed approach based on the 4D-CT is specific, quantitative diagnostics and it is the next step after the diagnosis of ECG.

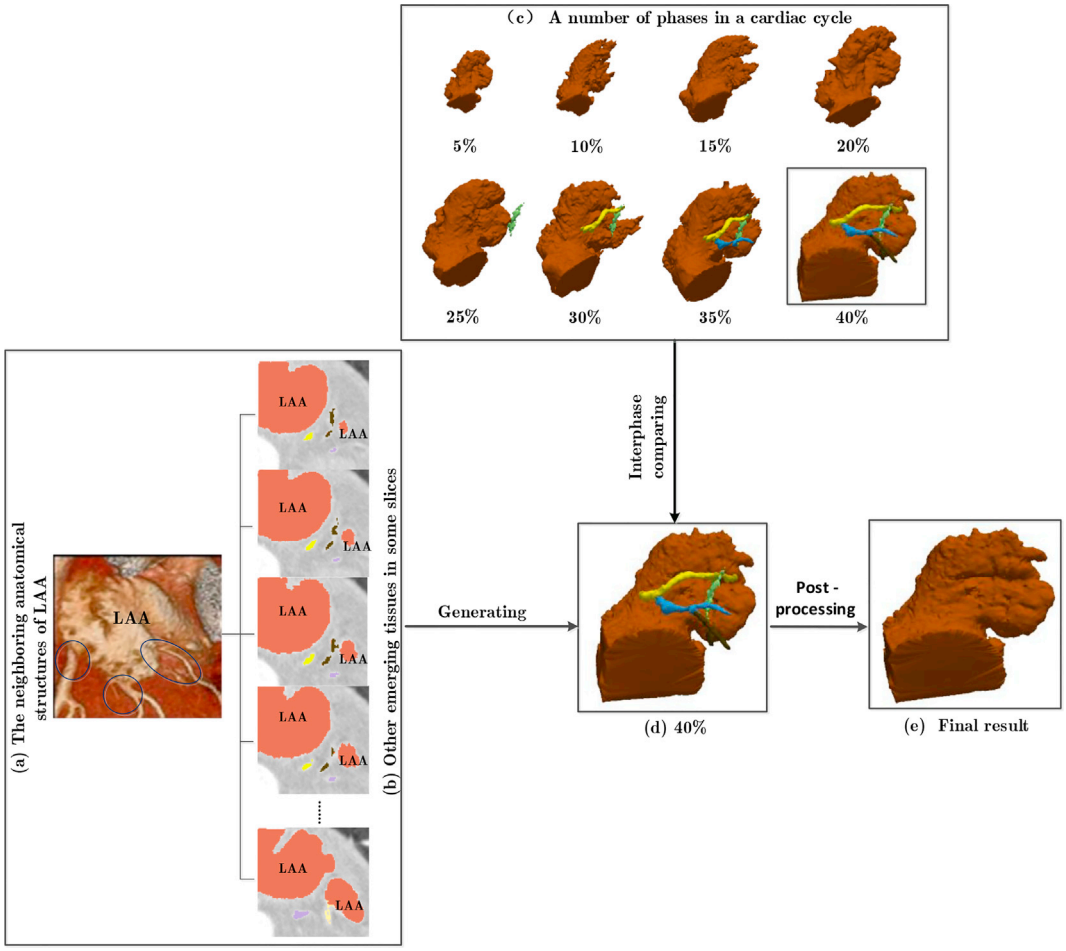

Fig. 12. Removal of neighboring interferences by multi-phase assisting segmentation. (a) The neighboring anatomical structures of the LAA, the left circumflex branches (LCXs) are marked with the circles. (b) Other emerging tissues in some slice, the red patches belong to the LAA, and the other color patches belong to the LCXs. (c) A number of phases in a cardiac cycle, the neighboring interferences do not occur in most of phases. (d) The rough segmentation result. (e) Final result. (For interpretation of the references to color in this figure legend, the reader is referred to the Web version of this article.)

Table 1
Volumetric changes of LAA in 100 patients in a entire cardiac cycle ($\overline{x} \pm s$).

Phase	Volume (ml)	Phase	Volume (ml)
5%	3.32 ± 1.23	55%	6.93 ± 2.79
10%	4.21 ± 1.18	60%	6.69 ± 2.61
15%	5.02 ± 1.69	65%	6.37 ± 2.51
20%	3.92 ± 1.89	70%	6.42 ± 2.66
25%	6.44 ± 2.18	75%	6.46 ± 2.24
30%	4.08 ± 2.23	80%	6.61 ± 2.31
35%	7.93 ± 2.48	85%	6.13 ± 2.06
40%	8.29 ± 2.70	90%	4.82 ± 1.71
45%	8.51 ± 2.93	95%	3.61 ± 1.31
50%	7.72 ± 2.84		

5.6.2. Multivariate logistic regression analysis for the risk of LAA thrombosis

Clinical data of 100 patients were collected, including age, gender, duration of AF, coronary disease, cardiomyopathy, hypertension, LAAV-max, LAAV-min, LAA-EF and LAA-PEF. Patients were divided into two groups: LAAT (LAA thrombi) group and no obvious abnormal group. The two groups were compared by two independent samples *t*-test, the two sample rates were compared using the chi-square test. In single factor analysis, the factors of $p < 0.1$ entered the multivariate logistic regression analysis, with the bilateral $p < 0.05$ as the difference to have the statistical significance. Statistical processing is based on SPSS Statistics 25 software. In single factor analysis, the differences of age, long-term PAF, hypertension, cardiomyopathy, LAAV-max, LAAV-min, LAA-EF and LAA-PEF were statistically significant ($p < 0.05$) (Table 4), especially LAA-EF in AF patients with LAAT was significantly reduced compared with those in AF without LAAT (12.9 ± 7.7 and $36.1 \pm 13.7\%$, respectively, $p < 0.001$); LAA-PEF in AF patients with LAAT are significantly reduced compared with those in AF without LAAT (23.9 ± 7.9 ml/s and 44.8 ± 15.4 ml/s, respectively, $p < 0.001$). The elements ($p < 0.1$) in the single factor analysis were brought into multivariate logistic regression analysis. From the results (Table 5), long-term PAF, cardiomyopathy, LAAV, LAA-EF, LAA-PEF are independent risk factors for the formation of LAAT. Especially LAAV, LAA-EF, LAA-PEF are the strongest predictor. Compared with the CHADS2 score and its updated version, the CHA2DS2-VASc score (frequently-used clinical prediction rules for estimating the risk of stroke in patients with AF) [51,52], volume-based LAA-EF and LAA-PEF provide a reasonable way to explore new risk stratification for stroke caused by LAAT.

An example (Male, 57 years old) is listed as shown in Fig. 16 and Table 6, from which we observe:

- The "volume - phase" curve is relatively gentle (called "Stunning");
- The LAA-EF is less than 35%;
- $\text{LAA-PFF}_1 < 20$ ml/s, $\text{LAA-PEF}_1 < 25$ ml/s, $\text{LAA-PFF}_2 < 15$ ml/s, $\text{LAA-PEF}_2 < 35$ ml/s (In an entire cardiac cycle, LAA-PFF_1 is the first peak filling flux; LAA-PEF_1 is the first peak emptying flux; LAA-PFF_2 is re-peak filling flux; LAA-PEF_2 is re-peak emptying flux).

The results of LAA-EF and LAA-PEF suggest that there is a high risk of

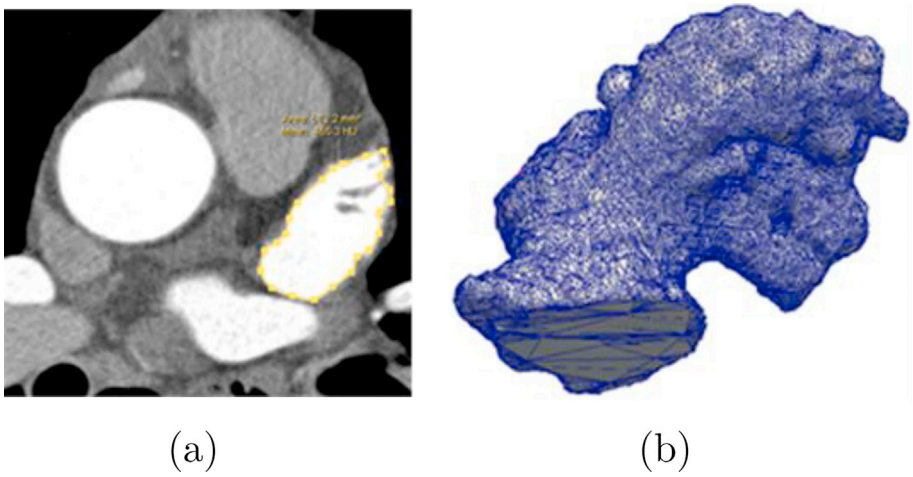

Fig. 13. (a) A tracked CT maximum LAA slice in single cardiac cycle. The region in yellow frame is maximum LAA patch in certain phase. (b) 3-D mesh surface model of a LAA in certain phase. (For interpretation of the references to color in this figure legend, the reader is referred to the Web version of this article.)

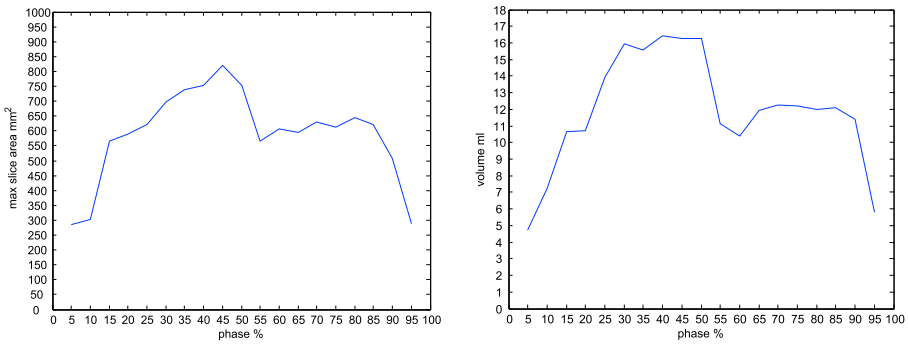

Fig. 14. An example of normal heartbeat. (a) The "max slice area-phase" curve. (b) The "volume-phase" curve.

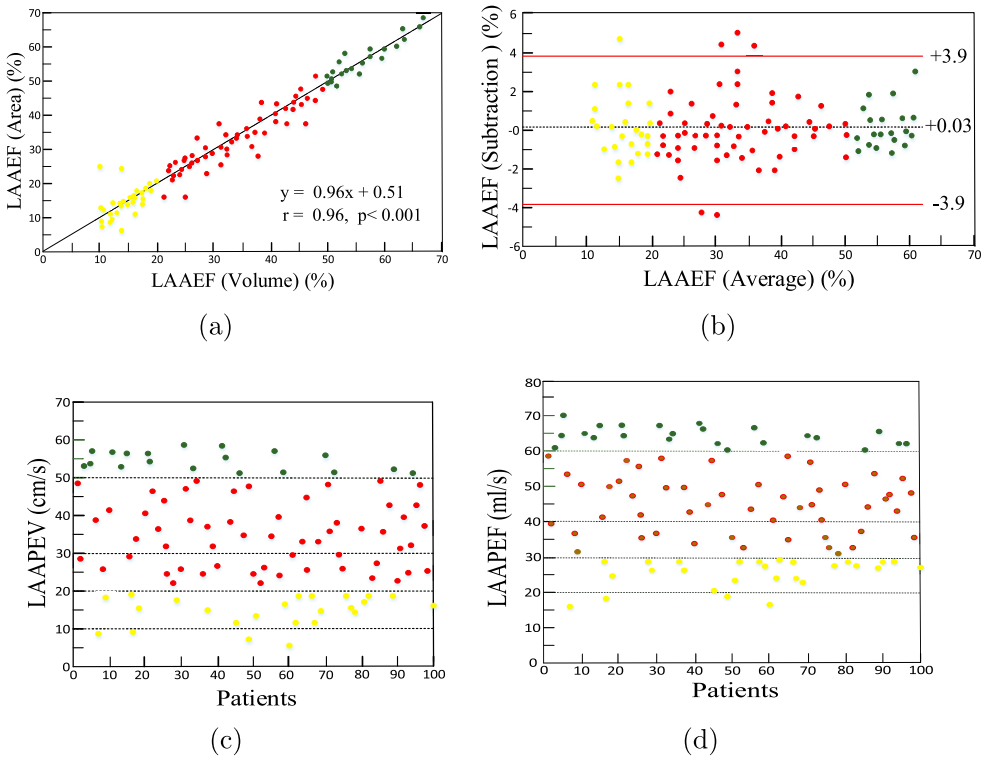

Fig. 15. Comparison between the "Single maximal slice area" and "Volume" method. The green, red, yellow dots represent approximate scattered distributions of the risk causing AF, and inducing cardiac thrombi from mild to serious for the corresponding parameters [46]. (a) Comparison of the left atrial appendage emptying fraction (LAA-EF) between the "Single maximal slice area" and "Volume" method in AF. (b) Bland and Altman plot. (c) The LAA-PEV by "Single maximal slice area" of 100 patients. (d) The LAA-PEF by "Volume" of 100 patients. In (c) and (d), the horizontal axis represents the serial number of 100 patients. And the dotted lines represent the division line of the corresponding scale, which don't mean classification. (For interpretation of the references to color in this figure legend, the reader is referred to the Web version of this article.)

Table 2
55 sets of training samples (numbers represent corresponding cases).

	NAF	PAF	CAF	Total
Training	12	26	17	55

Table 3
45 sets of testing samples (numbers represent corresponding cases).

	NAF	PAF	CAF	Total
Original diagnosis (ECG)	10	23	12	45
Auto-diagnosis diagnosis (4D-CT)	10	22	13	45

Table 4
Comparison of parameters of AF patients with LAAT and normal group.

	LAAT (n = 21)	Normal (n = 57)	p-value
Age (year, $\overline{x} \pm s$)	60.3 ± 9.8	55.7 ± 11.9	0.021
Male (case)	14	31	0.062
Duration of AF (year $\overline{x} \pm s$)	4.3 ± 5.9	4.9 ± 5.3	0.372
Long-term PAF (case)	5	24	< 0.001
Coronary disease (case)	3	23	0.032
Cardiomyopathy (case)	4	11	< 0.001
Hypertension (case)	6	57	0.004
LAAV-max (ml $\overline{x} \pm s$)	7.52 ± 4.93	6.61 ± 1.93	< 0.001
LAAV-min (ml $\overline{x} \pm s$)	5.79 ± 1.29	3.12 ± 1.26	< 0.001
LAA-EF (% $\overline{x} \pm s$)	12.9 ± 7.7	36.1 ± 13.7	< 0.001
LAA-PEF (ml/s $\overline{x} \pm s$)	23.9 ± 7.9	44.8 ± 15.4	< 0.001

Table 5
Multivariate logistic regression analysis of LAAT in patients with AF.

Variables	Odds ratio	95% confidence interval	p-value
Long-term PAF	1.012	1.003–1.987	0.003
Cardiomyopathy	1.031	1.013–2.013	0.007
LAAV-max	1.064	1.001–1.852	0.002
LAAV-max	1.029	1.012–1.981	0.003
LAA-EF	1.129	1.069–1.173	< 0.001
LAA-PEF	1.087	1.051–1.121	< 0.001

LAAT for this patient with AF [53,54]. Hence the diastolic function of LAA is abnormal, although it undergoes filling, emptying and re-filling, re-emptying in the entire cardiac cycle and satisfies the general conditions of " $\text{LAA-PEF}_2 > \text{LAA-PFF}_1 > \text{LAA-PEF}_1 > \text{LAA-PFF}_2$ " [48,55]. It is consistent with his previous diagnostic report: the clinical symptoms of this patient include heart palpitations, fainting, chest pain, and headache etc; the Halter (the 24-h electrocardiographic follow-up system) showed the irregularly narrow complex tachycardia, AF at approximately 157 beats per minute, and absentation of P wave; LAA filling defect (the LAAT. Fig 16 b) was found on cardiac CT examination. Furthermore, the CHA_2DS_2-VAS_c Score is 3, annual stroke risk is 3.2% [51,52]. In the 100 cases of data, there are some cases whose "volume-phase" curve of this example, the chief distinguishing features of which are that the base value turns larger and the curve turns more gentle. This phenomenon is called "Stunning". When "Stunning" happens, the flow velocity of blood is reduced to form thrombosis easily. Analysis of the "volume-phase" curve generated from 4-D CT data may be a non-invasive and convenient method for AF diagnosis.

6. Conclusion

We propose an LAA segmentation algorithm based on a ranking segmentation hypotheses generated by a parametric max-flow solver. The proposed approach is automated, except for the manual marking of a bounding box containing the LAA defined by four fiducial points. Owing to the fact that adjacent phases of 4-D CT images have similar topological relations, we take full advantage of temporal dimension information to segment the swaying LAA for each phase. Furthermore, to assist the diagnosis of AF, we calculate the volume of 3-D models, generate the "volume-phase" curve, and obtain the important dynamic metrics: LAA-PFF, LAA-PEF, and LAA-EF of the LAA based on the volume. Finally, we apply SVM to achieve an auto-diagnostics of AF and multivariate logistic regression analysis for the risk of LAA thrombosis.

The proposed segmentation approach can quickly and robustly segment multi-phases LAAs in batches, including LAA neck and lobes. It can be extended to the segmentation of tissues and organs with motion characteristics, and can also be used in the processing of other 4-D data, such as 4-D MR and ultrasound imaging.

We introduce the volume change ratio to calculate the key functional parameters of the LAA. Using these parameters to achieve quantitative diagnosis of AF, it visually reflects some physical characteristics of the lesion, and can provide complementary information to ECG in diagnosis of AF. Furthermore, by multivariate regression analysis shows that LAAV, LAAEF and LAA-PEF based on volume calculation are the significant risk factors for the formation of LAAT in patients with AF. This prediction of stroke risk is superior to the currently widely used $CHADS_2$ and CHA_2DS_2-VAS_c.

A limitation of the proposed approach is that the bounding box needs

Table 6
The LAA-PFF and LAA-PEF in each stage of a cardiac cycle, the LAA-EF (Male, 57 years old).

Volume	Phase	5% – 50%	50% – 65%	65% – 75%	75% – 100%
	LAA-PFF(ml/s)	15.78		9.375	
	LAA-PEF(ml/s)		19.17		31.52
	LAA-EF(%)			31.52	

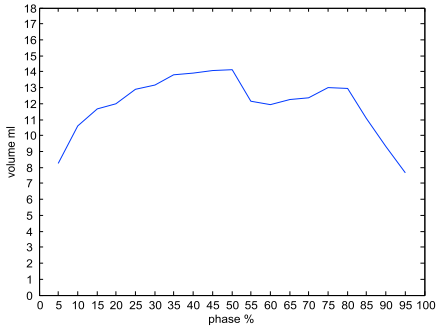

(a)

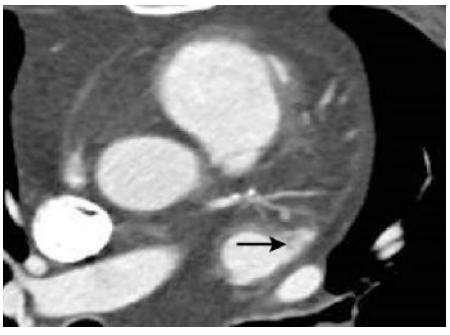

(b)

Fig. 16. The patient presented with LAAT in AF, male, aged 57 years. (a) The phenomenon of LAA "Stunning". (b) Filling defect in the LAA (the black arrow points to the LAAT).

to be manually calibrated, albeit with only four landmark points. The next step should be to find a way to automatically locate the LAA, e.g. by utilizing the relative position of the aorta and LAA. Another improvement is that the research can be further validated by using more experimental data, especially the 4-D data of other modality as a comparison, e.g. 3-D transesophageal echocardiography.

Conflicts of interest

None Declared.

References

[1] M. Yamamoto, Y. Seo, N. Kawamatsu, K. Sato, A. Sugano, T. Machino-Ohtsuka, R. Kawamura, H. Nakajima, M. Igarashi, Y. Sekiguchi, Complex left atrial appendage morphology and left atrial appendage thrombus formation in patients with atrial fibrillation, Circulation Cardiovascular Imaging 7 (2) (2014) 337–343.

[2] N.M. Alsaady, O.A. Obel, A.J. Camm, Left atrial appendage: structure, function, and role in thromboembolism, Heart 82 (5) (1999) 547–554.

[3] M. Taina, R. Vanninen, P. Sipola, A. Muuronen, P. JÄKÄLÄ, M. Hedman, Cardiac CT differentiates left atrial appendage thrombi from circulatory stasis in acute stroke patients, In Vivo 30 (5) (2016) 671–676.

[4] J.-W. Ha, B.-K. Lee, H.-J. Kim, W.-B. Pyun, K.-H. Byun, S.-J. Rim, N. Chung, Assessment of left atrial appendage filling pattern by using intravenous administration of microbubbles: comparison between mitral stenosis and mitral regurgitation, J. Am. Soc. Echocardiogr. 14 (11) (2001) 1100–1106.

[5] Y. Zheng, D. Yang, M. John, D. Comaniciu, Multi-part modeling and segmentation of left atrium in C-arm CT for image-guided ablation of atrial fibrillation, IEEE Trans. Med. Imag. 33 (2) (2014) 318–331.

[6] P. Grasland-Mongrain, J. Peters, O. Ecabert, Combination of shape-constrained and inflation deformable models with application to the segmentation of the left atrial appendage, in: IEEE International Symposium on Biomedical Imaging: from Nano to Macro, 14-17 April, 2010, pp. 428–431. Rotterdam, the Netherlands.

[7] P. Grasland-Mongrain, Segmentation of the Left Atrial Appendage from 3D Images, Master Thesis, ENS Cachan, 2009.

[8] R. Bolli, E. Marbán, Molecular and cellular mechanisms of myocardial stunning, Physiol. Rev. 79 (2) (1999) 609–634.

[9] T. Tabata, T. Oki, A. Iuchi, H. Yamada, K. Manabe, K. Fukuda, M. Abe, N. Fukuda, S. Ito, Evaluation of left atrial appendage function by measurement of changes in flow velocity patterns after electrical cardioversion in patients with isolated atrial fibrillation, Am. J. Cardiol. 79 (5) (1997) 615–620.

[10] O. Ecabert, J. Peters, H. Schramm, C. Lorenz, J. von Berg, M.J. Walker, M. Vembar, M.E. Olszewski, K. Subramanyan, G. Lavi, et al., Automatic model-based segmentation of the heart in CT images, IEEE Trans. Med. Imag. 27 (9) (2008) 1189–1201.

[11] T.Y. Law, P.A. Heng, Automated extraction of bronchus from 3D CT images of lung based on genetic algorithm and 3D region growing, Proceedings of SPIE - The International Society for Optical Engineering 3979 (2000) 906–916.

[12] Y. Boykov, G. Funka-Lea, Graph cuts and efficient nd image segmentation, Int. J. Comput. Vis. 70 (2) (2006) 109–131.

[13] V. Kolmogorov, Y. Boykov, C. Rother, Applications of parametric maxflow in computer vision, in: 2007 IEEE 11th International Conference on Computer Vision, IEEE, 2007, pp. 1–8.

[14] J. Carreira, C. Sminchisescu, Cpmc: automatic object segmentation using constrained parametric Min-cuts, IEEE Trans. Pattern Anal. Mach. Intell. 34 (7) (2012) 1312–1328.

[15] D.S. Hochbaum, The pseudoflow algorithm: a new algorithm for the maximum-flow problem, Oper. Res. 56 (4) (2008) 992–1009.

[16] L. Wang, J. Feng, et al., Left atrial appendage segmentation based on ranking 2-D segmentation proposals, in: Proceeding of MICCAI Workshop on Statistical Atlases and Computational Models of the Heart (STACOM), 2016, pp. 21–29.

[17] N. Baka, C. Metz, C. Schultz, L. Neefjes, R.J. van Geuns, B.P. Lelieveldt, W.J. Niessen, T. van Walsum, M. de Bruijne, Statistical coronary motion models for 2D+ t/3D registration of x-ray coronary angiography and cta, Med. Image Anal. 17 (6) (2013) 698–709.

[18] G. Piella, M. De Craene, C. Butakoff, V. Grau, C. Yao, S. Nedjati-Gilani, G.P. Penney, A.F. Frangi, Multiview diffeomorphic registration: application to motion and strain estimation from 3D echocardiography, Med. Image Anal. 17 (3) (2013) 348–364.

[19] A. Gomez, A. de Vecchi, M. Jantsch, W. Shi, K. Pushparajah, J.M. Simpson, N.P. Smith, D. Rueckert, T. Schaeffter, G.P. Penney, 4D blood flow reconstruction over the entire ventricle from wall motion and blood velocity derived from ultrasound data, IEEE Trans. Med. Imag. 34 (11) (2015) 2298–2308.

[20] K. Müller, A.K. Maier, P. Fischer, B. Bier, G. Lauritsch, C. Schwemmer, R. Fahrig, J. Hornegger, Left ventricular heart phantom for wall motion analysis, in: 2013 IEEE Nuclear Science Symposium and Medical Imaging Conference (2013 NSS/MIC), IEEE, 2013, pp. 1–4.

[21] N. Yoshida, M. Okamoto, H. Hirao, K. Nanba, H. Kinoshita, H. Matsumura, Y. Fukuda, H. Ueda, Role of transthoracic left atrial appendage wall motion velocity in patients with persistent atrial fibrillation and a low $CHADS^2$score, J. Cardiol. 60 (4) (2012) 310–315.

[22] G. Patti, V. Pengo, R. Marcucci, P. Cirillo, G. Renda, F. Santilli, P. Calabrò, A.R. De Caterina, I. Cavallari, E. Ricottini, et al., The left atrial appendage: from embryology to prevention of thromboembolism, Eur. Heart J. 38 (12) (2016) 877–887.

[23] M. Babenko, J. Derryberry, A. Goldberg, R. Tarjan, Y. Zhou, Experimental evaluation of parametric max-flow algorithms, in: International Workshop on Experimental and Efficient Algorithms, Springer, 2007, pp. 256–269.

[24] P. Arbelaez, M. Maire, C. Fowlkes, J. Malik, From contours to regions: an empirical evaluation, in: Computer Vision and Pattern Recognition, 2009. CVPR 2009. IEEE Conference on, IEEE, 2009, pp. 2294–2301.

[25] R. Wolz, C. Chu, K. Misawa, K. Mori, D. Rueckert, Multi-organ abdominal CT segmentation using hierarchically weighted subject-specific atlases, in: International Conference on Medical Image Computing and Computer-assisted Intervention, Springer, 2012, pp. 10–17.

[26] A.M.A. Lorza, D.D. Carvalho, J. Petersen, A.C. van Dijk, A. van der Lugt, W.J. Niessen, S. Klein, M. de Bruijne, Carotid artery lumen segmentation in 3D free-hand ultrasound images using surface graph cuts, in: International Conference on Medical Image Computing and Computer-assisted Intervention, Springer, 2013, pp. 542–549.

[27] A. Liaw, M. Wiener, et al., Classification and regression by randomforest, R. News 2 (3) (2002) 18–22.

[28] M. Wertheimer, Laws of Organization in Perceptual Forms.

[29] D.J. Williams, M. Shah, A fast algorithm for active contours and curvature estimation, CVGIP Image Underst. 55 (1) (1992) 14–26.

[30] X. Chen, J. Wang, Breast volume measurement by mesh projection method based on 3D point cloud data, Int. J. Cloth. Sci. Technol. 27 (2) (2015) 221–236.

[31] R. Keys, Cubic convolution interpolation for digital image processing, IEEE Trans. Acoust. Speech Signal Process. 29 (6) (1981) 1153–1160.

[32] M. Kass, A. Witkin, D. Terzopoulos, Snakes: active contour models, Int. J. Comput. Vis. 1 (4) (1988) 321–331.

[33] P.P. Teixeira, M.M. Oliveira, R. Ramos, P. Rio, P.S. Cunha, A.S. Delgado, R. Pimenta, R.C. Ferreira, Left atrial appendage volume as a new predictor of atrial fibrillation recurrence after catheter ablation, J. Intervent. Card Electrophysiol. (2017) 1–7.

[34] W.K. Jeong, J.-H. Choi, J.P. Son, S. Lee, M.J. Lee, Y.H. Choe, O.Y. Bang, Volume and morphology of left atrial appendage as determinants of stroke subtype in patients with atrial fibrillation, Heart Rhythm 13 (4) (2016) 820–827.

[35] R.S. Breiman, J.W. Beck, M. Korobkin, R. Glenny, O.E. Akwari, D.K. Heaston, A.V. Moore, P.C. Ram, Volume determinations using computed tomography, Am. J. Roentgenol. 138 (2) (1982) 329–333.

[36] I.M. Singh, D.R. Holmes, Left atrial appendage closure, Curr. Cardiol. Rep. 12 (5) (2010) 413–421.

[37] T. Sahin, D. Ural, T. Kilic, U. Bildirici, G. Kozdag, A. Agacdiken, E. Ural, Evaluation of left atrial appendage functions according to different etiologies of atrial fibrillation with a tissue Doppler imaging technique by using transesophageal echocardiography, Echocardiography 26 (2) (2009) 171–181.

[38] R. Topsakal, N.K. Eryol, İ. Özdoğru, E. Seyfeli, A. Abaci, A. Oğuzhan, E. Başar, A. Ergin, S. Çetin, Color Doppler tissue imaging to evaluate left atrial appendage function in patients with mitral stenosis in sinus rhythm, Echocardiography 21 (3) (2004) 235–240.

[39] N.K. Eryol, R. Topsakal, B. Kıranatlı, A. Abacı, Y. Çiçek, A. Ouzhan, E. Başar, A. Ergin, S. Çetin, Color Doppler tissue imaging to evaluate left atrial appendage function in mitral stenosis, Echocardiography 20 (1) (2003) 29–35.

[40] C.-M. Yu, F. Fang, Q. Zhang, G.W. Yip, C.M. Li, J.Y.-S. Chan, L. Wu, J.W.-H. Fung, Improvement of atrial function and atrial reverse remodeling after cardiac resynchronization therapy for heart failure, J. Am. Coll. Cardiol. 50 (8) (2007) 778–785.

[41] M. Anselmino, M. Scaglione, L. Di Biase, S. Gili, P. Santangeli, L. Corsinovi, M. Pianelli, F. Cesarani, R. Faletti, D. Righi, et al., Left atrial appendage morphology and silent cerebral ischemia in patients with atrial fibrillation, Heart Rhythm 11 (1) (2014) 2–7.

[42] P.J. Besl, N.D. McKay, et al., A method for registration of 3-D shapes, IEEE Trans. Pattern Anal. Mach. Intell. 14 (2) (1992) 239–256.

[43] Y. Chen, G. Medioni, Object modelling by registration of multiple range images, Image Vis Comput. 10 (3) (1992) 145–155.

[44] T. De Potter, S. Chatzikyriakou, E. Silva, G. Van Camp, M. Penicka, A pilot study for left atrial appendage occlusion guided by 3-dimensional rotational angiography alone, JACC Cardiovasc. Interv. 11 (2) (2018) 223–224.

[45] C.T. January, L.S. Wann, J.S. Alpert, H. Calkins, J.C. Cleveland, J.E. Cigarroa, J.B. Conti, P.T. Ellinor, M.D. Ezekowitz, M.E. Field, et al., 2014 AHA/ACC/HRS guideline for the management of patients with atrial fibrillation, Circulation 130 (23) (2014) 199–267.

[46] M. Iwama, M. Kawasaki, R. Tanaka, K. Ono, T. Watanabe, T. Hirose, M. Nagaya, T. Noda, S. Watanabe, S. Minatoguchi, Left atrial appendage emptying fraction assessed by a feature-tracking echocardiographic method is a determinant of thrombus in patients with nonvalvular atrial fibrillation, J. Cardiol. 59 (3) (2012) 329–336.

[47] C.-W. Hsu, C.-J. Lin, A comparison of methods for multiclass support vector machines, IEEE Trans. Neural Network. 13 (2) (2002) 415–425.

[48] Y. Matsumoto, Y. Morino, A. Kumagai, M. Hozawa, M. Nakamura, Y. Terayama, A. Tashiro, Characteristics of anatomy and function of the left atrial appendage and their relationships in patients with cardioembolic stroke: a 3-dimensional transesophageal echocardiography study, J. Stroke Cerebrovasc. Dis. 26 (3) (2017) 470–479.

[49] J. Weston, C. Watkins, et al., Support vector machines for multi-class pattern recognition, in: Esann, vol. 99, 1999, pp. 219–224.

[50] K.-B. Duan, J.C. Rajapakse, M.N. Nguyen, One-versus-one and one-versus-all multiclass SVM-RFE for gene selection in cancer classification, in: European Conference on Evolutionary Computation, Machine Learning and Data Mining in Bioinformatics, Springer, 2007, pp. 47–56.
[51] R.K. Sandhu, J.A. Bakal, J.A. Ezekowitz, F.A. McAlister, Risk stratification schemes, anticoagulation use and outcomes: the risk–treatment paradox in patients with newly diagnosed non-valvular atrial fibrillation, Heart 97 (24) (2011) 2046–2050.
[52] S.H. Hohnloser, G.Z. Duray, U. Baber, J.L. Halperin, Prevention of stroke in patients with atrial fibrillation: current strategies and future directions, Eur. Heart J. Suppl. 10 (suppl_H) (2008) H4–H10.
[53] N. Güler, R. Demirbağ, C. Özkara, B. Eryonucu, A. Güneş, M. Tuncer, Ü. Güntekin, S. Kocabaş, M. Agirbasli, Clinical and echocardiographic predictors of left atrial appendage dysfunction in patients with mitral stenosis in sinus rhythm, J. Am. Soc. Echocardiogr. 17 (8) (2004) 819–823.
[54] S. Qamruddin, J. Shinbane, J. Shriki, T.Z. Naqvi, Left atrial appendage: structure, function, imaging modalities and therapeutic options, Expet Rev. Cardiovasc. Ther. 8 (1) (2010) 65–75.
[55] S. Kumar, F. Sutherland, M. Wheeler, P.M. Heck, G. Lee, A.W. Teh, M.L. Garg, J.G. Morgan, P.B. Sparks, Effects of chronic omega-3 polyunsaturated fatty acid supplementation on human atrial mechanical function after reversion of atrial arrhythmias to sinus rhythm: reversal of tachycardia-mediated atrial cardiomyopathy with fish oils, Heart Rhythm 8 (5) (2011) 643–649.